Tuning the Structure and Conductivity of Carbon-Elastomer Composites

Dissertation

zur Erlangung des Grades

des Doktors der Ingenieurwissenschaften

der Naturwissenschaftlich-Technischen Fakultät

der Universität des Saarlandes

von

Long Zhang

Saarbrücken

2023

Tag des Kolloquiums: 2. Mai 2024

Prodekan: Prof. Dr.-Ing. Michael Vielhaber

Berichterstatter: Professor Dr. Tobias Kraus
Professorin Dr. Karen Lienkamp

Akad. Mitglied: Dr.-Ing. Andreas Tschöpe

Vorsitz: Prof. Dr.-Ing. Markus Gallei

Acknowledgments

During my stay in Germany, I was fortunate to receive assistance from numerous individuals. I am grateful and aim to express my appreciation in languages and document their acts of kindness.

I would like to thank my supervisor, Prof. Dr. Tobias Kraus, for his help in designing the study topics and methods, and also for his help and generosity during my time in the group.

I would like to thank Dr. Lola González-García and Dominik Schmidt from the Electrofluids group who worked with me to complete some of the work.

I would like to thank our collaborators, Prof. Dr. Tanja Schilling and Fabian Coupette from the University of Freiburg, for the fruitful discussions and informative exchanges during the meetings.

I would like to thank my colleagues in the Structure Formation Group, especially Dr. Peihua Yang, Dr. Louis Weber, Dr. David Doblas-Jimenez, Dr. Björn Kuttich, Anna Zimmermann, Indra Beckes, Andrea Pyttlik, Selim Basaran and Lukas Engel, with whom I really enjoyed working.

I would like to thank Robert Strahl, Sarah Schumacher, Aron Schorr, and Robert Drumm for their help in performing numerous tests.

Finally, I would like to thank Prof. Dr. Karen Lienkamp for serving as my second referee and for her constructive suggestions in correcting the dissertation.

Statement on Contributions

I performed all of the experiments and measurements presented in this dissertation except those listed below.

Transmission electron microscopy (TEM) investigations were performed by Dr. Louis Weber from the Leibniz Institute for New Materials (INM) in Saarbrücken, Germany.

Surface adsorption measurements were performed by Sarah Schumacher from the INM in Saarbrücken, Germany.

Ultra-small-angle X-ray scattering (USAXS) measurements were performed by Andrei Chumakov from the Deutsches Elektronen-Synchrotron DESY in Hamburg, Germany. The USAXS data were analyzed by Dr. Dr. Björn Kuttich and Long Zhang from the INM in Saarbrücken, Germany.

Optical microcopy and rheology tests were conducted and analyzed by Dominik Schmidt and Long Zhang from the INM in Saarbrücken, Germany.

Publication Report

Publication 1

Coupette, F.; Zhang, L.; Kuttich, B.; Chumakov, A.; Roth, S.; González-García, L.; Kraus, T.; Schilling, T., "Percolation of rigid fractal carbon black aggregates", *J. Chem. Phys*. **2021***,* 155, 124902.

https://doi.org/10.1063/5.0058503

Contribution of Long Zhang: sample preparation for testing; experimental conduction except for TEM imaging and USAXS measurements; experimental data analysis; drafting and revision of the manuscript.

The experimental results from this publication have been used in Chapter 3. The wording and description have been changed to fit the structure of the dissertation.

Publication 2

Zhang, L.; Schmidt, S.; González-García, L.; Kraus, T., "Microscopic Softening Mechanisms of an Ionic Liquid Additive in an Electrically Conductive Carbon-Silicone Composite", *Adv. Mater. Technol.* **2022**, 7, 2101700.

https://doi.org/10.1002/admt.202101700

Contribution of Long Zhang: sample preparation for testing; experimental conduction; experimental data analysis, drafting and revision of the manuscript.

The results from this publication have been used in Chapter 4. The wording and description have been changed to fit the structure of the dissertation.

Abstract

In this work, I studied composites made of polydimethylsiloxane (PDMS) and carbon black (CB). This dissertation will focus on the fundamental issue of network formation of CB fillers with different size distributions. The percolation thresholds of composites using different sizes CB is compared to understand how the aggregate arrangement in agglomerates will affect the percolation and electrical conductivity of the composites. The influence of fillers' structure on electrical conductivity is analyzed on multiple length levels. The fractal dimensions of filler agglomerates in composites change as a function of filler concentrations as shown via ultra-small-angle X-ray scattering.

The microstructural changes caused by adding the ionic liquid (IL) 1-ethyl-3-methylimidazolium bis(trifluoromethylsulfonyl)imide to PDMS-CB composites are analyzed to explain the electrical, mechanical, rheological, and optical properties of IL-containing precursors and composites. Swelling experiments and optical analysis indicate a limited solubility of the IL in the PDMS matrix and reduction of the cross-linking density of PDMS both globally and locally, which reduced the Young's Moduli of the composites. Rheological analysis of the precursor mixture shows that the IL reduces the strength of carbon-carbon and carbon-PDMS interactions, thus lowering the filler-matrix coupling and increasing the elongation at break. Electromechanical testing reveals a combination of reversible and irreversible resistance changes consistent with IL's presence at microscopic CB-CB interfaces.

Zusammenfassung

In dieser Arbeit untersuche ich Komposite aus Polydimethylsiloxan (PDMS) und Leitruß (Carbon Black, CB). Der Fokus liegt auf grundlegenden Fragen der Netzwerkbildung von CB Füllern unterschiedlicher Größenverteilungen. Die Perkolationsschwellen von Kompositen mit CB unterschiedlicher Größen werden verglichen, um zu verstehen, wie die Anordnung von Aggregaten Perkolation und elektrische Leitfähigkeit der Komposite beeinflusst. Der Einfluss der Füllstoffstruktur auf verschiedenen Längenskalen auf die elektrische Leitfähigkeit wird auf verschiedenen Längenskalen analysiert. Die fraktale Dimension von Füllstoffagglomeraten in den Kompositen ändert sich mit dem Füllgrad, wie Untersuchungen mittels Ultrakleinwinkelröntgenstreuung zeigen.

Die Änderungen der Mikrostruktur durch Beigabe der -Ethyl-3-methylimidazolium-bis(trifluoreomethylsulfonyl)imid zu PDMS-CB Kompositen wird untersucht, um die elektrischen, mechanischen, rheologischen und optischen Eigenschaften der IL enthaltenden Vorstufen und Kompositen zu erklären. Experimente zur Quellung und optische Analysen deuten auf eine begrenzte Löslichkeit der IL in der PDMS-Matrix und eine lokale und globale Reduktion der Vernetzung des PDMS hin, die den Elastizitätsmodul der Komposite verringern. Die rheologische Analyse der Vorstufen zeigt, dass die IL die CB-CB und CB-PDMS Wechselwirkungen verringert und so die Kopplung zwischen Füllstoff und Matrix und die Dehnbarkeit erhöht. Elektromechanische Tests zeigen eine Mischung aus reversiblen und irreversiblen Widerstandsänderungen, die mit der Anwesenheit von IL an mikroskopischen CB-CB Grenzflächen konsistent sind. Elektromechanische Tests zeigen eine Mischung reversibler und irreversibler piezoelektrischer Antworten, die mit der Anwesenheit von IL an mikroskopischen CB-CB Grenzflächen konsistent sind.

Table of Contents

1 Introduction

1.1 Motivation

Improved human-machine interaction requires new materials that combine the good electrical performance of today's rigid circuits with mechanical properties that mimic human skin. Elastomer composites reinforced with conductive fillers have attracted considerable interest due to their flexibility and tunable electrical properties.[1-3] Pure elastomers are limited by their low electrical conductivity and mechanical strength. By mixing with conductive fillers such as metal particles, carbon materials and semiconductor materials, the electrical properties of elastomer composites can be improved when the conductive filler content reaches a critical volume fraction, the percolation threshold.[4-6] The conductive network formed by fillers in the polymer matrix is important for the electrical conductivity of elastomer composites. The size and shape of fillers and their distribution in the polymer matrix also affect the electrical properties of elastomer composites.[7] For the same polymer matrix, different fillers such as carbon blacks (CBs), carbon nanotubes (CNTs) and metal particles will result in different percolation thresholds.[8] And by using different mixing methods to change the distribution of fillers in the polymer matrix, the percolation thresholds will also be varied.[9] It should also be noted that if the concentration of conductive fillers is too high, the composite will become inflexible and difficult to handle, as the mechanical properties will be different from those of the pure polymer matrix. It is therefore important to achieve the proper concentration in these elastomer composites to obtain satisfactory electrical and mechanical properties.

Materials that respond electrically to mechanical deformation, or vice versa, can be used as sensors and actuators. Recently, in response to the need for more elastic sensor and actuator materials, elastomer-carbon particle composites have become the focus of research.[10-12] Ultra-sensitive electromechanical sensors have been created by combining graphene and viscoelastic polymers.[13] However, despite the long industrial experience with CB, research activities have focused on CNTs and graphene, because their carbon structures are much better defined than CB. Their simple geometries have facilitated the analysis of structure-property relationships and allowed researchers to model the electrical behavior of the composite, and related simulation work is well established.[4, 14-28] Unlike graphene or CNT, CB has complex shapes as shown in Figure 1.1. And CB particles form weaker agglomerates that are randomly distributed throughout the elastomer matrix, making it difficult to analyze the conductive network formed by such structures.[29]

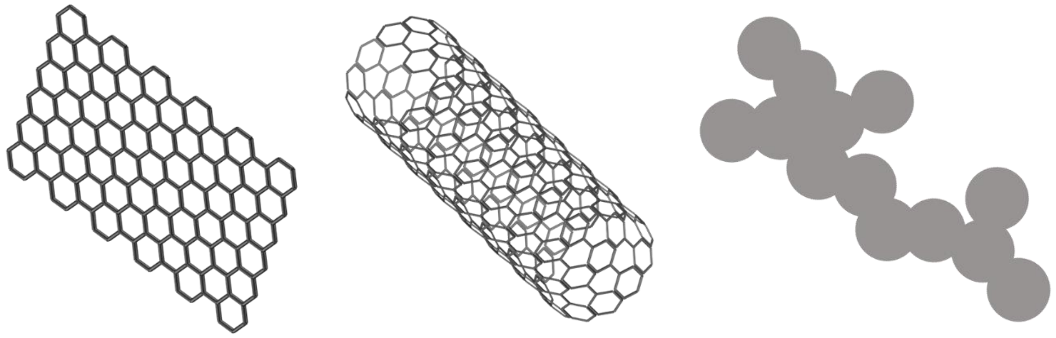

Figure 1.1. Structure examples of graphene, carbon nanotube (CNT) and carbon black (CB).

Here we proposed that it is not necessary to use highly defined carbon nanostructures to obtain elastomer-carbon nanocomposites with high electrical conductivities that are mechanically strong and respond to mechanical deformation with well-defined electrical responses. CB is also suitable for making such materials, while avoiding the complex and costly processes required for CNTs and other nanostructures. However, although CBs are more industrially available, there are still problems associated with their use as fillers. One is that

CBs are more widely distributed in size, and the fractal structures of CB aggregates and agglomerates in the polymer matrix are less well understood. It is important to understand the charge transport properties of fractal objects under mechanical stress. This is a topic that has not been sufficiently studied, perhaps due to the complex structure of such particles. Another is the problem of the elastomer becoming less soft due to the addition of fillers.

1.2 Carbon Black

Carbon black (CB) refers to several industrial products, including thermal, furnace and acetylene blacks. They essentially consist of elemental carbon in the form of near spherical particles of colloidal size, coalesced into particle aggregates.[30-31] Approximately 90 % of CB production is used by the tire industry to modify fracture behavior and improve abrasion and failure properties.[32] CB is also used as a filler in elastomers to modify mechanical, electrical and optical properties.

As shown in Figure 1.1, the shape and structure of carbon black is more difficult to describe than that of CNT and graphene. In order to achieve the desired properties and understand the CB conductive network formed in the polymer matrix, the structure of CB should first be known. The following sections introduce the hierarchical structure of CB and methods for describing such structures.

1.2.1 Primary Particle, Aggregate and Agglomerate

The schemes of CB primary particle, aggregate and agglomerate are shown in Figure 1.2. Warren first studied the microstructure of CB by X-ray diffraction in 1934.[33] He concluded that CB is not a true amorphous form of carbon, but is composed of small crystallites consisting of parallel graphitic layers. Primary particles typically range in size from 10 to 100 nm.[34] Transmission electron microscopy (TEM) remains one of the most feasible methods for measuring the primary particle size distributions of CBs, although the problem of defining particle boundaries is not easy to overcome. Liquids such as chloroform and toluene have been found to be suitable dispersants for CBs when used in conjunction with ultrasonic separation.[35-37] Particle diameters should be measured manually on micrographs and a histogram plotted to derive the distribution curve.

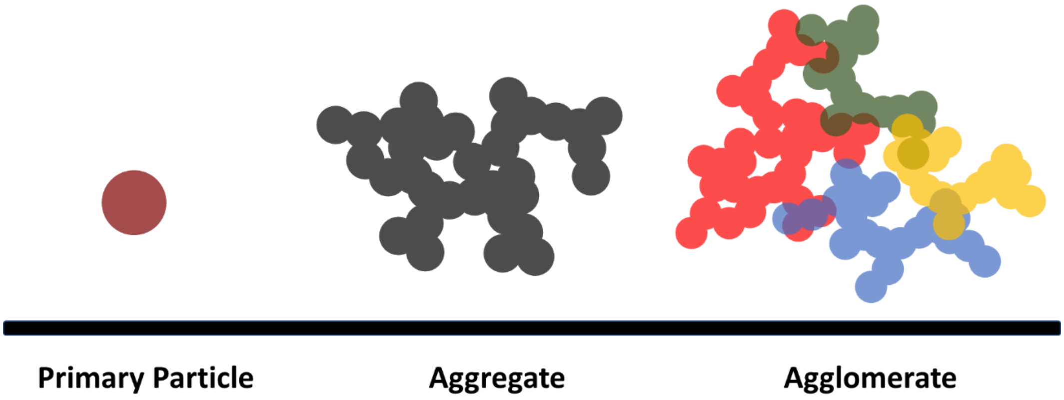

Figure 1.2. Schematic of primary particles, aggregate and agglomerate.

CB primary particles rarely exist in an isolated form. Instead, they form aggregates of various sizes. During the CB formation stage, aggregates form as individual particles that adhere to other particles and are then “fused” together by the deposition of additional carbon from the gas stream. CB aggregates are considered the smallest dispersible unit, and a primary particle can only be separated from an aggregate by fracturing. The size and shape of the aggregates are important primary properties of CBs. The size of the aggregates can vary from hundreds of nanometers to several microns in average size for different types of CBs.[38] Similar to the analysis of primary particle size distributions, TEM has been widely used to study the morphology of CB aggregates. Gruber et al. investigated the distribution properties of CB aggregates by imaging the aggregates at different goniometer angles using TEM. Individual aggregates exhibited maximum area and perimeter when the goniometer angle was near 0°, and higher structure aggregates were found to show greater relative changes in morphological observations with rotation than lower structure aggregates.[39] However, it should be noted that due to the nature of the irregular shape of CB aggregates, measuring the size of CB aggregates based on electron microscopy images is time consuming and the development of an improved method of dimensional analysis is needed to fully characterize the morphology and size of CB.

Surface area is a powerful index for understanding the "size" of CB aggregates. Surface area provides no distributional information, and the surface area value has only an inverse correlation with particle/aggregate size. Adsorption methods based on nitrogen, cetyltrimethylammonium bromide, and iodine are widely used to measure specific surface area (SSA). The Brunauer-Emmett-Teller (BET) theory is used to calculate the SSA of solids or porous materials.[40-41] Unlike the Langmuir model[41], which assumes that adsorption is limited to a monolayer, the BET model allowed for multilayer adsorption and was still able to determine the number of molecules of the adsorbate that formed a monolayer. For a more detailed introduction to BET theory, see Section 2.1.

CB aggregates can form a larger structure. Various functional groups such as hydroxyl or carboxyl groups are found on the surface of CB. Therefore, the CB aggregates tend to agglomerate due to the nature of the CB surface.[42] The aggregates in agglomerates are bound together by van der Waals forces and have difficulty maintaining their integrity during processing.[43] Because these agglomerates are loosely bound, it is difficult to know the exact morphologies of the agglomerates. It is also difficult to distinguish between aggregates and agglomerates because the size distributions of aggregates can be broad, and the size distributions of agglomerates can partially coincide with those of aggregates.

1.2.2 Fractal Geometries of Carbon Black

As shown in Figure 1.2, CB aggregates and CB agglomerates have complex structures, and such structures are known as fractal structures. Mandelbrot first introduced fractal geometry in 1975, and this idea was first officially published in 1977.[44] In conventional Euclidean geometry, a surface is described by a power of two and a volume by a power of three. However, these criteria cannot be applied to objects with complex structures. Self-similarity is the essential characteristic of fractal objects, which refers to an infinitely self-repeating structure at all scales. Natural forms and patterns are often random fractals, since they are composed of random patterns or shapes that occur randomly on some length scale. This means that their self-similarity can only be observed statistically. Therefore, non-integer dimensions, also called fractal dimension, are important for describing fractal objects.

Due to the manufacturing process, the geometries of many materials such as CB are difficult to define in the real world. Irreversible clustering of tiny particles is a key topic in scientific fields.[45] This type of growth occurs when a chemical species precipitates from a supersaturated matrix or is subjected to further heat treatment. Several models, such as diffusion-limited aggregation (DLA), cluster-cluster aggregation (CCA), and ballistic aggregation (BA), have been developed and used to describe colloid formation.[46] According to Witten, "DLA is an idealization of the process by which matter irreversibly combines to form dust, soot, dendrites and other random objects in the case where the rate-limiting step is diffusion of matter to the aggregate."[45] Therefore, it makes sense to use the DLA model to describe the CB aggregate as well. In the following section, the DLA and CCA models are discussed to help the reader understand the fractal structures of the CB aggregate and CB agglomerate.

Diffusion-Limited Aggregation (DLA) Model

The diffusion-limited aggregation (DLA) model has been used to describe the fractal structures of CB, soot, dust, dendrites, etc. Witten and Sander developed the DLA growth model and showed how completely random motion can produce a self-similar pattern.[47] And this is the starting point of which fractal research activities multiplied. The model was developed under the stimulation of explaining experimental work by Forrest and Witten, which proposed that fractal structure could be developed by aggregation of small particles in a dense gas.[48] Although this model does not fully match the experimental results, it is still a breakthrough in the study and description of fractal objects. Figure 1.3 shows a DLA cluster containing 5000 particles and gives a general description of what a DLA cluster looks like.

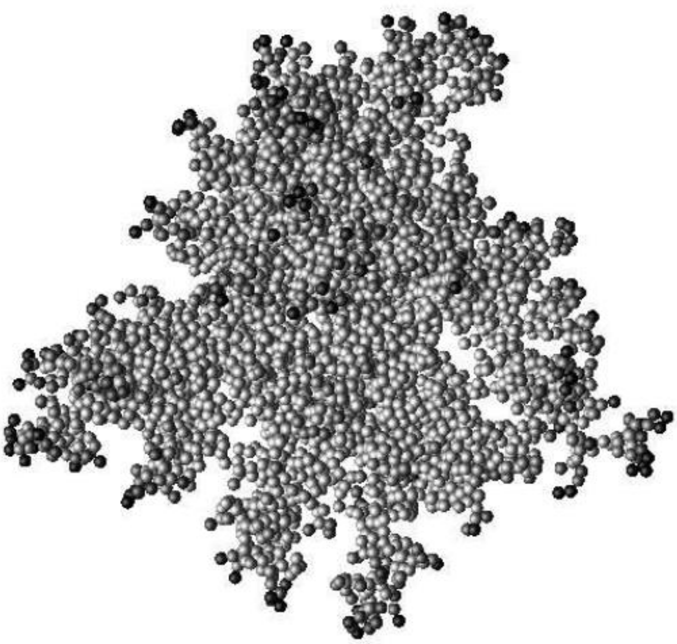

Figure 1.3. Schematic of a DLA cluster containing 5000 particles.[49] Reprinted with permission, open access. Copyright (2002), the National Academy of Sciences of Ukraine.

Figure 1.4 shows a schematic of the formation of a DLA cluster. One particle was fixed at the center of space, and the other particles were then introduced one by one at the starting radius R at a random angular position. The particle was allowed to move randomly until it either left space or joined the cluster at the center. In the latter case, it became part of the expanding objects. This process was repeated several times until the cluster was formed.

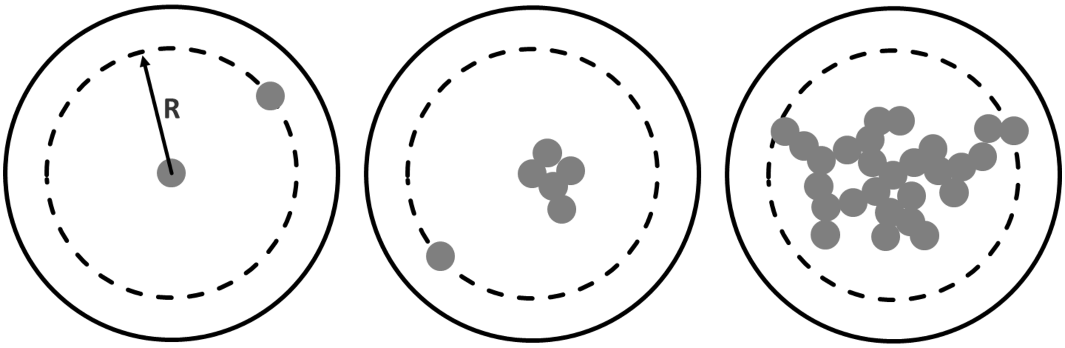

Figure 1.4. Schematic of DLA cluster formation.

The development process is very straightforward, but it still results in a branching pattern or self-similar structure. The fundamental explanation for the resulting self-similar structure is that the growth rule is nonlocal; however, it should be emphasized that nonlocality is not a necessary condition for producing such branching self-similar clusters.[46] The local structure of a self-similar fractal, which is larger than a few lattice units but overall much smaller than the overall size of the cluster can be expressed as

$$C(r) \sim {R_g}^{D_\alpha - d} \tag{1.1}$$

where r is the distance, $C(r)$ is the correlation function, R_g is the radius of gyration, D_α is the fractal dimension and d is the Euclidean dimensionality value of the embedding space.

The simulation results showed that, for a two-dimensional (2D) DLA cluster, the fractal dimension is about 1.7, and this value increases to 2.5 for a three-dimensional (3D) DLA cluster.[50]

Cluster-Cluster Aggregation (CCA) Model

The cluster-cluster aggregation (CCA) model is more commonly used to explain filler agglomeration in the polymer matrix. To develop a CCA model, as shown in Figure 1.5, two particles were initially selected from a basket containing N particles. At the beginning, one particle was fixed at the center of space and the other was introduced on the starting radius. The particle moved randomly until it either found the particle in the center or left space. If two particles joined, the new cluster was put back into the basket and the total number became N-1. If the particle went out of space, the random walk of the particle was aborted. In subsequent iterations, two objects were randomly taken from the basket and the random walk was performed again. This process was repeated until the final cluster was formed.

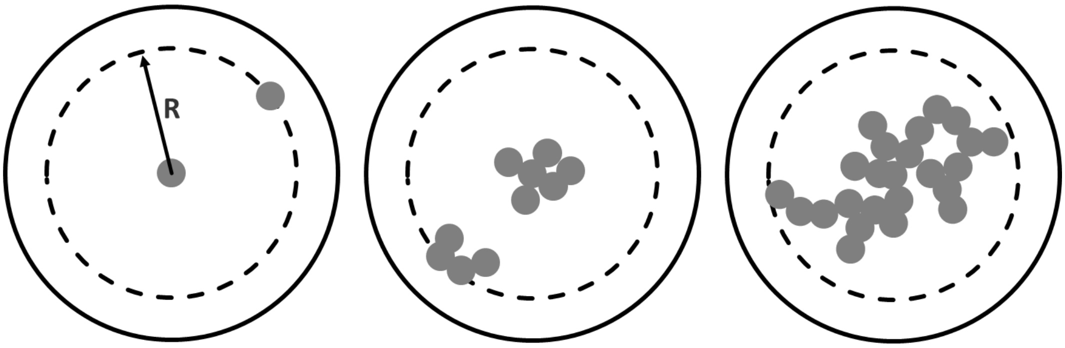

Figure 1.5. Schematic of CCA cluster formation.

The model is based on the assumption that nanoscopic filler particles, such as CB, are not fixed in space but can perform random movements, i.e. the particles are allowed to fluctuate around their mean position in a polymer matrix. When adjacent particles or clusters come into contact, they stick together irreversibly. This refers to the fact that the thermal energy of colloidal particles is generally much smaller than their interaction energy. Due to the high viscosity of the polymer, the mobility of the particles is limited, but it increases significantly with decreasing particle size and increasing temperature as the viscosity decreases.[51]

1.2.3 Fractal Dimension

Section 1.2.2 illustrated the models that can describe fractal objects. This section introduces the concept of fractal dimension to numerically describe the structure of the fractal object. A fractal dimension is a ratio in fractal geometry that serves as a statistical measure of complexity by examining how the complexity in a pattern varies with its measured scale. Unlike dimensions in Euclidean space, a fractal dimension need not be an integer, and the fractal dimension is not as intuitive and self-explanatory as the integer dimension. A fractal dimension can be thought of as a measure of the ability of a pattern to fill space, expressing the differences between the fractal scale and the space in which it is embedded.

Kahnert et al. presented a clear comparison of aggregates with different fractal dimensions.[52] As shown in Figure 1.6, all 4 types of aggregates contain 500 primary particles. Aggregates a and b both have a fractal dimension $d_f = 1.8$, and the fractal dimension of c and d is 2.4. The aggregates with lower fractal dimension are more linear than the aggregates with higher fractal dimension. The difference between the aggregates a and b is caused by the fractal pre-factor. The pre-factor can be interpreted as a measure of the compactness of the aggregate branches. Aggregates c and d have the same fractal dimension and pre-factor. However, aggregate c was constructed using the CCA model, while aggregate d was constructed using the DLA model. Aggregates c and d look similar, and c appears to have a more homogeneous distribution of particles throughout the aggregate.

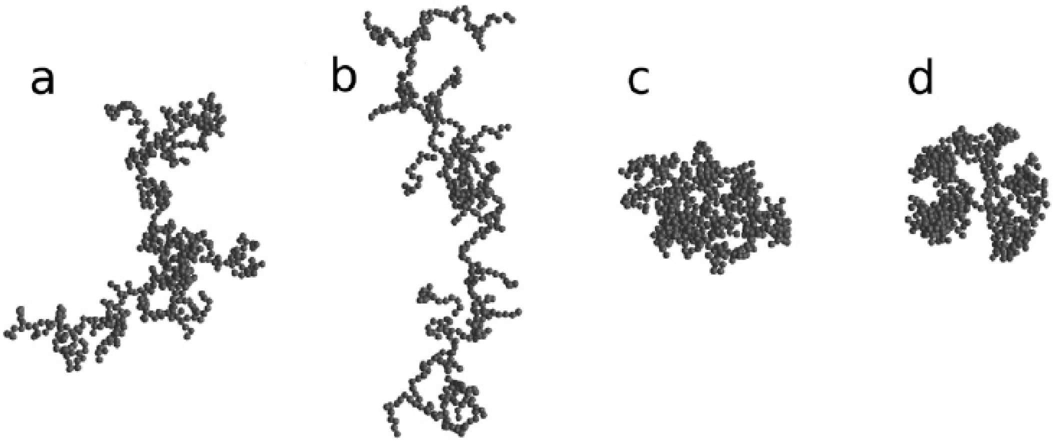

Figure 1.6. Aggregates with varying fractal dimension. a and b, d_f =1.8, c and d, d_f =2.4. Geometries a–c were generated with the cluster-cluster aggregation (CCA) algorithm, geometry d was produced with the diffusion-limited aggregation (DLA) algorithm [52] Reprinted with permission, open access. Copyright (2020), Elsevier.

As shown in Figure 1.7, two types of fractal structures can exist simultaneously in a fractal object, one is the fractal structure colored in red, which reflects the complexity of the surface, called the surface fractal; the other is the mass fractal, which is associated with the packing efficiency of an aggregate. Both surface and mass fractal structures have a fractal dimension, so it is important to distinguish between the concepts of surface fractal and mass fractal to properly describe the fractal object.

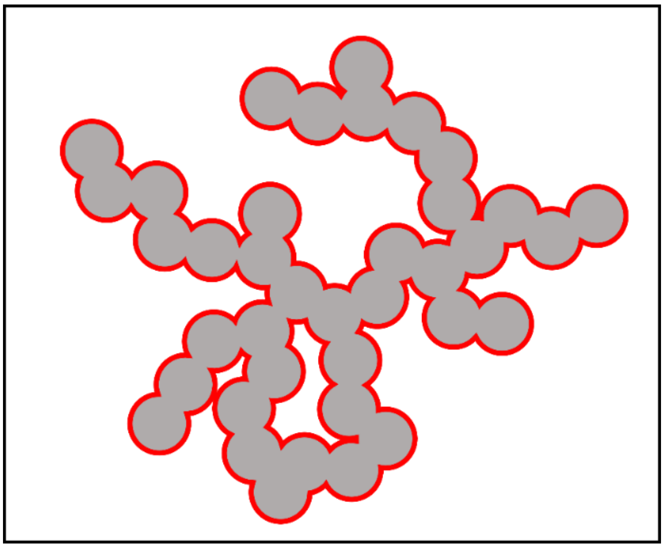

Figure 1.7. Schematic of surface fractal (red) and mass fractal (gray).

Small-angle scattering (SAS) is a well-established technique for probing the nano/micro scale structure in fractal materials.[32, 53-56] Both surface and mass fractal dimensions can be obtained from log-log plots of $I(q)$versus q ,where q is the scattering vector, $I(q)$ is the scattering intensity from the SAS measurements. For a more detailed introduction to scattering data analysis, see Section 2.4.

The surface fractal dimension d_s illustrates how the surface of the object grows with the size of the object. The scattering from a surface fractal object is that

$$I(q) \sim q^{-(6-d_s)} \tag{1.2}$$

Meaningful values of d_s are in the interval $2 \leq d_s < 3$. Thus, a reasonable value of the exponent for a surface fractal is $3 < 6 - d_s \leq 4$.

For natural surfaces, the fractal dimension is directly related to surface roughness in an intuitive way: an almost smooth fractal surface has a fractal dimension slightly greater than 2 because it tends to flatten out over a classically modeled surface; conversely, an extremely rough surface has a fractal dimension close to 3 because it tends to fill a volume.[57]

The mass fractal dimension d_m represents how the structure's mass scales with its size, and the scattering intensity $I(q)$ of a mass fractal also follows a power law as shown in equation (1.3).

$$I(q) \sim q^{-d_m} \tag{1.3}$$

The dimension of a mass fractal is always less than the dimension of the space in which it is embedded, and the value of d_m will be $1 \leq d_m \leq 3$. As a fractal structure grows, its mass increases less rapidly than the volume it occupies. Therefore, the density of a fractal object is not constant, but decreases with increasing size.[58]

In practice, by analyzing different regimes, the critical power law exponent obtained from the scattering curve is the fractal dimension.[59] If the absolute value of the measured scattering exponent is less than 3, then the sample is a mass fractal with fractal dimension d_m in the measured q-range, and if the exponent is between 3 and 4, then the sample is a surface fractal with fractal dimension $6 - d_s$.[60]

Several publications have focused on studying the agglomeration behavior of solid fillers in the polymer matrix by analyzing the surface and mass fractal dimension of the fillers.

Rieker et al. tested nine commercially available CBs by small-angle X-ray scattering (SAXS) and pointed out that the mass fractal aggregates show three defining features in the $I\ (q)\ vs.\ q$ scattering data plotted on log-log scales: at high q values (shorter length scales), a power law region corresponding to surface scattering from the primary particles, a second power law region at lower q values (longer length scales) corresponding to scattering from the aggregates, and a curved crossover region between the two power laws. The authors concluded that the crossover point can be determined from experimental SAS data by plotting $-\mathrm{d}I/\mathrm{d}q\ vs.\ q$.[61] This crossover point depends on the mean diameter and size distribution of the primary particles that make up the aggregate. A Guinier analysis (see Section 2.2.2) of the crossover regions gives a significantly larger value for the mean particle diameter than that obtained by TEM.

By interpreting the fractal dimensions, Rieker et al. investigated the effect of processing on the agglomeration behavior of CB fillers in the high density polyethylene (HDPE) matrix using SAXS.[62] Both Brabender and solution methods were used to prepare CB/HDPE and CB/ethylene propylene rubber (EPR) composites, and multiple filler loading was used to prepare the composites in both methods. The authors observed that for the CB/HDPE composites prepared by the Brabender method, when the filler loading is above the percolation threshold, there is a continuous decrease in the mass fractal dimension values. However, for the CB/HDPE composites prepared by the solution method, the mass fractal dimension values are almost independent of the filler loading. This implies that both the polymer matrix and the mixing method have a great influence on the filler arrangement and, as a result, the composites may exhibit different electrical and mechanical properties.

Ehrburger-Dolle et al. made a further attempt to correlate the macroscopic behavior of the composites with the structure of the CB aggregate networks when altered by strain.[63] For uncross-linked EPR composites, the scattering pattern changed from isotropic to anisotropic when the strain increased to 0.27, and the pattern showed a “butterfly” shape when the strain was above 0.53. For the samples under strain of 0.53, the SAXS intensity curves measured along the direction parallel and perpendicular to the strain axis are no longer identical. As shown in Figure 1.8, the mass fractal dimension of 1.5 for the initial sample indicates that the CB aggregates formed a connected network of slightly interpenetrating aggregates. For $\varepsilon = 0.53$, the slope of -1.8 is similar to the value of isolated CB aggregates, and for the direction perpendicular to the strain, the aggregates are highly interpenetrated and give a slope of -1. However, no anisotropy was observed for the cross-linked composites. This indicates that cross-linking induces strong interpenetration of CB aggregates and formation of large agglomerates. In comparison, for the same amount of CB dispersed in SBR, the scattering behavior is isotropic for small strains, and a butterfly pattern was observed only when the strain was above 0.25. And after cross-linking, the scattering pattern remained almost isotropic. The results clearly showed that the agglomeration behavior of CB fillers is influenced by several parameters, such as the polymer matrix and the degree of cross-linking. [63]

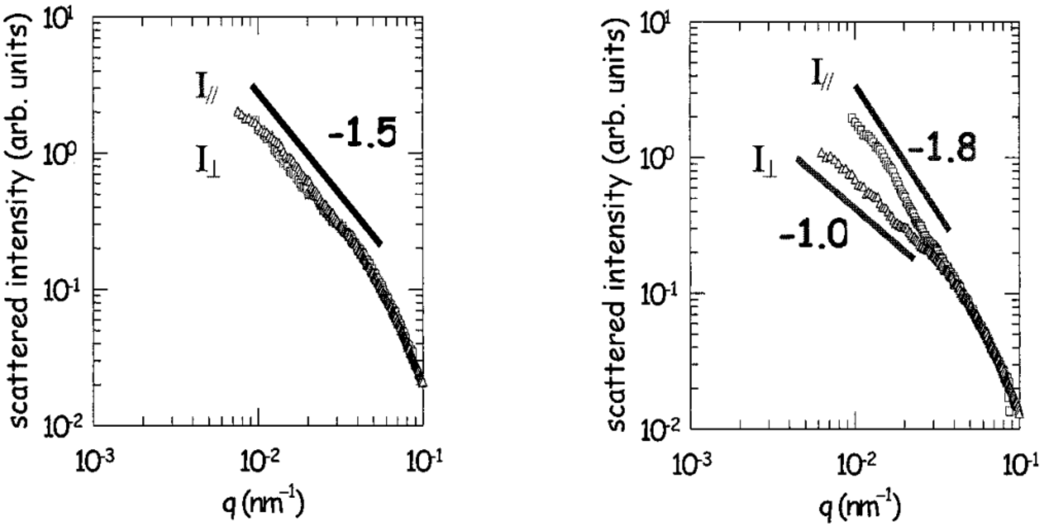

Figure 1.8. SAXS intensity curves determined along the two directions (parallel and perpendicular to the direction of stretch) for the initial sample (left) and the stretched sample ($\varepsilon =$ 0.53, right). Reprinted with permission. Copyright (2003), Wiley-VCH.

1.3 Elastomer Composites

Materials such as CB are usually in a powder state, which makes them difficult to use alone in a device. However, when used as conductive fillers in elastomers, composites have a wide range of applications in sensors and actuators. The next section summarizes some of the research results based on these elastomer composites.

1.3.1 Applications of Elastomer Composites

Elastomer composites have been extensively studied in human motion detection, health monitoring, stretchable and wearable strain sensors where flexibility, sensitivity and skin-friendliness are required.[64-78]

For example, Kunze et al. proposed a novel concept for a bendable planar soft robotic module driven by the intelligent artificial muscles. The intelligent artificial muscles consisted of silicone-based rolled dielectric elastomer actuator membranes[67] made of PDMS and CB, and a rigid top plate. The actuation is provided by an antagonist-agonist of the intelligent artificial muscles. The influence of the free design parameters on the bending angle performance was reported by both situation and experiment.[68-69]

Sang et al. investigated the effect of CNT morphology on the properties of polyurethane composites for strain sensors. A lower percolation threshold and higher gauge factor (GF) can be obtained by using CNTs with branched morphology. The GF of the sensor was further increased to 350 at 200 % strain. Application examples for finger and wrist were also presented to show the high potential of branched CNT as a filler for the strain sensor material.[79]

Zhu et al. proposed a novel flexible capacitive tactile sensor based on CB/PDMS and CNT/PDMS materials. The authors systematically investigated the sensitivity of the sensor in terms of detecting applied forces from different directions, and a mathematical model of force and capacitance variance was established to predict the value of the applied force. Regarding the CB/PDMS dielectric materials, the authors also mentioned that with increasing loading of CB fillers, the Young's modulus increases and the flexibility of the composite is affected, which has a negative impact on the sensitivity of the sensor.[80]

In contrast to the classic stretchability and sensitivity studies, Nankali et al. focused their studies on the effect of environmental factors (i.e., changes in temperature and relative humidity) on the strain sensing properties of the highly stretchable sensors. The authors systematically reported the performance of CNT-PDMS strain sensors under controlled environmental conditions. Overall, the sensors showed good durability with an elongation within 60 % and low hysteresis behavior under both small and large strains. Temperature variations had a significant effect on the strain sensing behavior. As the temperature increased from 27 °C to 65 °C, the normalized base resistance of the sensor decreased by 65 % and the GF decreased from 10 to 4.[81]

Lee et al. proposed a novel highly flexible and stretchable strain sensor based on silver nanoparticles (Ag NPs) patterned on PDMS stamps. The opening/closing of micro-cracks under mechanical deformation causes the resistance change. The change in normalized resistance ranged from 0.06 to 0.41 as the strain increased from 5 % to 20 %. The sensor was sensitive to both tension and compression, making it suitable for detecting finger flexion and wrist rotation.[82]

Feng et al. investigated several stretchable patterned circuits using conductive composite composed of Ag NPs and PDMS. The stretchability and electrical properties of patterns including rhombuses, straight lines, serpentines, triangles, ellipses, and folds were investigated. It was pointed out that the rhombus-pattern circuits exhibited stable electrical conductivity when subjected to very high tensile strains, and it maintained good conductivity after over 10000 strain-relief cycles from 0 % to 150 %. It is promising for use as a next-generation strain sensor and wearable artificial skin.[83]

Other particles such as aluminum nanoparticles and ferroelectric $BaTiO_3$ nanoparticles, have also been used to prepare elastomer composites for sensors and actuators.[84-85]

1.3.2 Elastomer Composites Modified by Ionic Liquids

An ideal elastomer composite should be able to withstand large deformations while remaining conductive and mechanically stable over many cycles. However, the addition of conductive fillers has long been known to significantly increase the stiffness of elastomers.[86-93] The basic requirement for reinforcement is to achieve a homogeneous dispersion of fillers in the elastomer matrix, resulting in good interphase adhesion. However, the agglomeration of fillers during the mixing process makes it difficult to achieve a homogeneous dispersion in the polymer. Both high loading and heterogeneous filler dispersion have a negative effect on the performance of elastomer composites. In recent years, ILs have been increasingly used in the field of elastomer science as additives to tune the electrical and mechanical properties of composites. Several studies have focused on how the IL affects the dispersion of fillers in the polymer matrix and the material properties.[94-101]

ILs have been shown to modify the surface of fillers such as silica, CNTs. and CB, resulting in improved dispersion in the polymer matrix. Das et al. tested 5 types of ILs to improve the interaction between rubber and CNT fillers. Among the candidate ILs, 1-allyl-3-methyl-imidazolium chloride (AMIMCl) was able to increase the elongation of the composite of solution-styrene-butadiene rubber (S-SBR) and polybutadiene rubber (BR) with 3 wt-% CNTs up to 456% without mechanical failure. Interestingly, the addition of AMIMCl resulted in higher electrical conductivity compared to the use of CNTs alone.[99]

Kreyenschulte et al. continued the work of Das by studying the interactions of AMIMCl with different grades of CB using a combination of rheological measurements, differential scanning calorimetry and Raman spectroscopy. The authors concluded that it is most likely that the attractive interactions between CB and AMIMCl are provided by the cations of the IL and the π-electrons of graphitic structures on the CB surface.[100]

Hassouneh et al. reported the use of 1-ethyl-3-methylimidazolium bis(trifluoromethanesulfonyl)imide [EMIM][TFSI] to improve the dispersion of CNT in the PDMS matrix and investigated the conductivities of the composites as a function of mixing sequence and method. Both dispersion aids and effective mechanical mixing methods are required to obtain a high conductivity elastomer, and speeding mixing combined with a roll mill method was found to be an effective approach to preparing the high conductivity composites.[102]

Narongthong et al. focused on CB-filled SBR.[103-104] The authors concluded that IL 1-decyl-3-methyl imidazolium chloride (DMIC) improves the degree of filler dispersion, reduces the number of large agglomerates and increases the number of conductive paths, resulting in improved electrical conductivity and sensitivity. The sensitivity of the composite sample with an IL/CB mass ratio of 1.5 was approximately 600 % higher at 2.5 % stain than the samples without IL. And the sensitivity increased up to 700 % at 9 % strain compared to the samples without IL. The addition of IL makes the composites more deformable and highly responsive to small strains, making them suitable for small-strain sensors.

These studies have highlighted the influence of ILs on the properties of composites, but little is known about the interaction between the elastomer matrix, fillers and ILs. It remains unclear how the addition of ILs to the composites alters the formation of the conductive networks and their changes under strain.

The composites mentioned in Section 1.3.1 and 1.3.2 exhibited good electrical and mechanical properties benefiting from the network formed by the filler material within the polymer matrix. And it is important to understand the formation of the conductive network in order to better design the composites and achieve the desired properties. Scattering techniques can provide localized structural information, but limited by their resolution, scattering techniques do not provide reliable information about the connectivity of the filler network on larger length scales. In the following section, percolation theory is introduced to illustrate the structure of filler networks and its application to understanding the conductivity of composites.

1.3.3 Percolation Theory in Elastomer Composites

Percolation is a theory that describes the properties associated with the connectivity of large numbers of objects. In general, percolation is the expression of network formation when nodes or links are added to the disordered system.[105] Percolation theory is thus related to graph and network theory. Figure 1.9 shows the percolation behavior of a system containing two types of elements. The yellow and blue elements are randomly distributed in the system, and when the upper and lower boundaries (in black color) are continuously connected by one type of element, this connection is called percolation. It has a wide range of applications, from transport behavior in amorphous and porous composites to the properties of branching polymers, gels, and complex ionic conductors.[106]

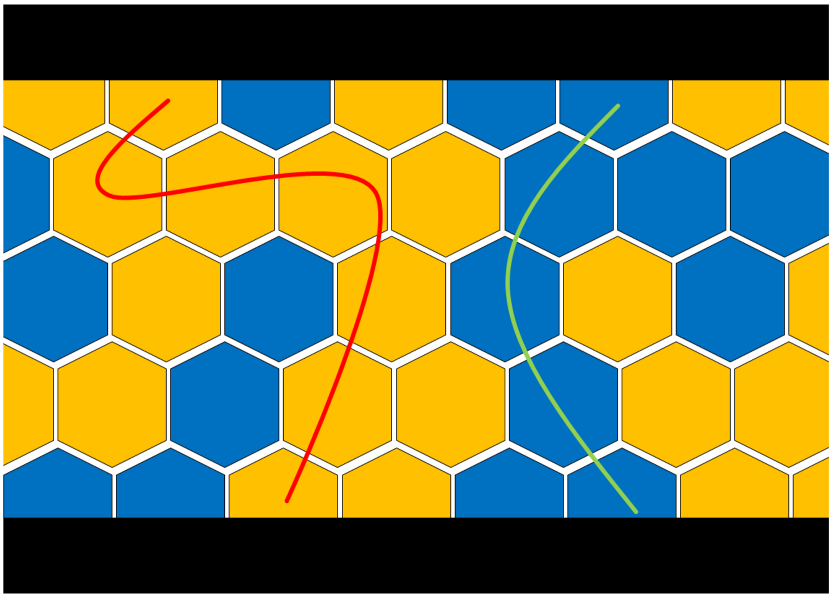

Figure 1.9. Schematic of percolation. The red and green lines represent the percolation paths of the yellow and blue elements, respectively.

Here is an explanation of how percolation occurs in a system. Consider a square lattice where each site was randomly occupied with probability P or unoccupied with probability $1 - P$. The occupied sites were separated or formed isolated small clusters at low concentrations p. If two occupied sites were adjacent, they merged into one. The connection of all occupied sites forms a path when the concentration p increases to a certain value, p_c. This critical value p_c is called the percolation threshold. Beyond the percolation threshold, paths are more likely to form, i.e. the probability of percolation path formation increases.

The relation between the probability P and the percolation threshold p_c can be described as

$$P \sim (p - p_c)^{\beta} \tag{1.4}$$

where β is the critical exponent.

Conductive fillers introduce conductivity into the insulating polymer matrix. To understand the electrical properties of composites introduced by fillers, the formation of the filler network in the polymer matrix should be studied. Percolation theory can be used to explain the transition of the composite from insulator to conductor as the conductive fillers increase, as shown in Figure 1.10.[107-108]

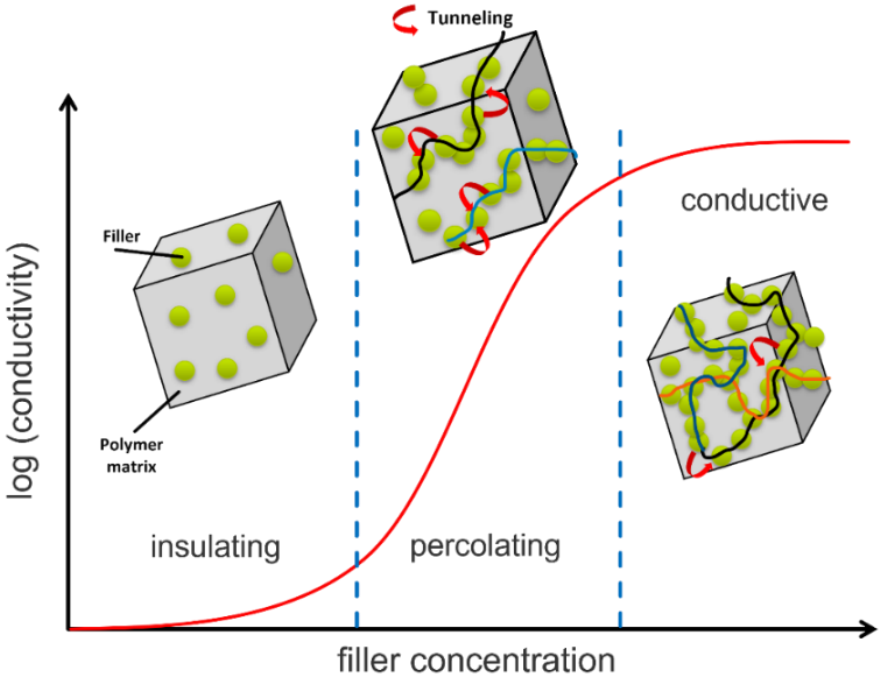

Figure 1.10. Schematic of a composite material in transition from an insulator to a conductor.

The percolation threshold is the point at which an insulating material becomes conductive. The concentration at which percolation occurs is called the critical concentration. Percolation theory makes it possible to predict the critical concentration and calculate the probability of connections between particles. The conductive behavior of a composite can be described as

$$\sigma \sim \sigma_0 (\varphi - \varphi_c)^t \tag{1.5}$$

where σ is the electrical conductivity of the composite, σ_0 is a prefactor, φ is the volume fraction, φ_c is the volume fraction corresponding to the percolation threshold and t is the critical power law exponent.

1.3.4 Influence of Filler Geometries on Network Formation

The structures of fillers have a significant influence on the formation of the conductive network in the polymer. As a result, the critical power law exponent and percolation threshold will be very different when using different types of fillers. For example, Dang et al. reported thermoplastic elastomer (TPE) composites filled with CB, CNT and CNT-CB. The critical power law exponents are 1.067, 4.5 and 4.63 for CB, CNT and CNT-CB filled TPE, respectively.[109] The critical power law exponent has been reported to have values of about 1.26 for two-dimensional systems and approximately 1.95 for randomly distributed three-dimensional structures.[110] In experiments, the observed critical power law exponents are always different from the theoretical value because real chemical systems contain structures on different competing length scales. Rubin et al. have shown that the non-universal value of the critical power law exponent of conductivity provides an indication of the role of carrier tunneling in the conduction mechanism of filled polymer composites, and in such a case a tunneling percolation model can describe the system better than the conventional model.[111] In this dissertation, the critical power law exponent is considered only as a fitting parameter without further discussion.

The shape of the fillers also has a significant effect on the percolation threshold. When monodisperse spherical materials are used as fillers, percolation theory predicts a critical volume fraction of about 30%.[112] The electrical conductivity of CNT composites and the formation of CNT conductive networks have been studied both experimentally and theoretically.[113-119] Taking advantage of the aspect ratio of CNTs, the percolation threshold can be as low as 0.11 vol-%.[117] It has been reported that the geometric threshold is a key factor in establishing a conductive network,[118] but others factors such as interphase, waviness and tunneling, also increase the probability of electron transfer in isotropic networks.[119]

Schilling et al. have performed several simulations of the percolation behavior of nanorods in terms of polydispersity, aspect ratio, etc. The authors have presented a theoretical and computer simulation using the Monte Carlo method to study the effects of polydispersity on geometrical percolation in suspensions of rod-like materials. The percolation threshold is insensitive to the type of size distribution, whether it is bi-disperse, Gaussian, or Weibull. When only the length polydispersity is considered, the percolation threshold is inversely proportional to the aspect ratio. In addition, the percolation threshold remains insensitive to aspect ratio when expressed in terms of the weight average.[14] Schilling et al. also introduced a new version of the connectedness percolation theory that can estimate percolation thresholds for nanorods over a wide range of aspect ratios, including those as small as 10.[120]

The percolation behavior of CBs in polymers has been widely reported experimentally. When CBs are used as fillers, the percolation threshold has been reported to be approximately between 4 vol-% and 20 vol-%.[51, 109, 121-123] This range is between those observed for CNT and spherical fillers. Klüppel summarized the percolation thresholds of emulsion polymerized styrene-butadiene rubber (E-SBR) composites using different grades of CB. The percolation threshold increased as the specific surface area (SSA) and solids content of the primary aggregates decreased. The author concluded that the kinetic aggregation process plays an important role, and the percolation thresholds increase with decreasing SSA mainly due to the restriction of mobility with decreasing SSA of the primary aggregates.[51]

In addition to the research directions focused on filler geometries, studies have also been conducted on the influence of the polarity of the polymer matrix on the structure formation of the composites[121, 124-125] and on how to achieve electrical conductivity with very little filler material[126-131]. For example, the percolation behavior of CBs in three types of resins was studied by Choi and co-workers.[121] In particular, the authors investigated the dependence of the percolation threshold on the polarity and crystallinity of the polymer. It was pointed out that when CB was mixed with a polymer of very high polarity, the inter-cohesion between the polymer and CB was very strong and hydrogen bonding occurred within the polymer resin, resulting in the prevention of current flow. Conversely, a non-polar and relatively weak-polar polymer resulted in good current flow and a low percolation threshold. Kontopoulou et al. showed that the induced polarization forces between the CBs lead to the formation of electrically conductive structures within the PDMS matrix, which was confirmed by rheological characterization coupled with admittance measurements.[127] Electron microscopy has also been used to study the distribution of CB fillers in the polymer matrix.[132-136] Jäger and his colleagues correlated the distribution studied by SEM with the fractal dimension.[137] These results are valuable in understanding the structure formation of fillers.

It should be noted that the results on CB are difficult to compare. One reason is that researchers used CBs from different sources and did not perform sufficiently detailed characterizations to describe the CBs. Another is that, in addition to differences in polymer matrix, mixing methods and fillers, researchers sometimes used additives to achieve desired electrical or mechanical properties, and the effect of these additives on CB network formation remains unclear.

1.4 Objective

The purpose of this dissertation is to discuss how to tune the properties of composites consisting of polydimethylsiloxane (PDMS) and CB, which can provide fundamental insight into the design of conductive composites with desired electrical and mechanical properties. Characterization methods that help to understand the materials and their properties are discussed in Chapter 2. The influence of CB aggregate size and their agglomeration on the conductivity of the elastomer composites is discussed in Chapter 3. To obtain the conductive composites with desired large deformation, the ionic liquid (IL) is used to tune the electrical and mechanical properties of the PDMS composites, and the interaction between the IL, CB, and PDMS is discussed in Chapter 4. Chapter 5 summarizes the results of this dissertation.

2 Methods

This chapter introduces the methods that will be used in Chapters 3 and 4 to characterize the structural properties of CB fillers, as well as the electrical, mechanical, rheological and swelling properties of the composites. The main characterization techniques and the analytical problems associated with them are discussed in this chapter. For a more detailed technical description, the reader is referred to other literature.

2.1 Nitrogen Adsorption Isotherm Measurement

Nitrogen adsorption isotherm measurement is performed to measure the specific surface area (SSA) and extract the fractal dimension of CB powders in Chapter 3.

Brunauer-Emmett-Teller (BET) theory is used to calculate the specific surface area (SSA) of solid or porous materials from nitrogen adsorption isotherm measurements. [40, 138] To determine the surface area, the solid sample is cooled under vacuum to cryogenic temperature (using liquid nitrogen). An adsorbate, such as nitrogen gas, is added to the solid sample in controlled increments. After each dose of nitrogen gas, the relative pressure P/P_0 is allowed to equilibrate. The BET equation describes the relationship between the volume of gas molecules adsorbed, V, at a given relative pressure, P/P_0. The volume of nitrogen adsorbed (V) is determined as

$$\frac{1}{V\left(\frac{P_0}{P}-1\right)}=\frac{1}{V_mC}+\frac{C-1}{V_mC}\times\frac{P}{P_0} \tag{2.1}$$

where V_m is the number of the nitrogen gas molecules required to form a monolayer (the adsorbent shown in purple color in Figure 2.1) and C is the BET constant related to the heat of adsorption.

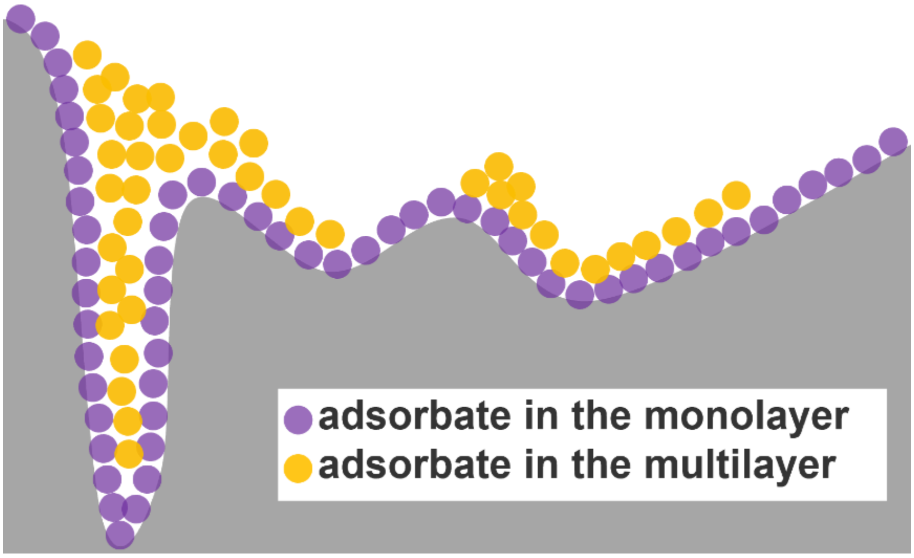

Figure 2.1. Schematic of monolayer and multilayer formation.

The BET equation shows a linear behavior of $1/((P_0/P)-1)$ $vs.$ P/P_0. From the plot, the volume of nitrogen V_m that forms a monolayer of surface area can be determined. The SSA of the sample can be calculated from the slope and intercept of the BET plot using the equation.

$$\text{SSA} = \frac{V_m N_a a_m}{v_m m_s} \tag{2.2}$$

where N_a is the Avogadro's number (6.022×10^{23} mol^{-1}), a_m is the effective cross-section area of one adsorbed molecule, v_m is the molar volume of one adsorbed molecule and m_s is the mass of substrate adsorbent.

In addition to deriving the SSA, nitrogen adsorption data can also be used to derive the fractal dimension of fractal materials.

The fractal dimension d can be predicted from the following fractal BET relation,

$$\frac{V}{V_m} \sim \left[1 - \frac{P}{P_0}\right]^{(d-3)} \tag{2.3}$$

where $d - 3$ is the slope of the log-log plot of V/V_m $vs.$ $(1 - P/P_0)$. The fractal BET relation is sensitive to the multiple-wall effect and equation (2.3) is only valid for mass fractal evaluation in the high pressure range.[138-139]

Compared to the fractal BET relation, the fractal Frenkel-Halsey-Hill (FHH) theory [140-141] is less sensitive to the multiple-wall effect and provides powerful predictions of fractal dimension.

$$\frac{V}{V_m} \sim \left[\ln\left(\frac{P_0}{P}\right)\right]^{(d-3)} \tag{2.4}$$

2.2 Analytical Centrifugation

Analytical centrifugation (AC) is used to determine the size distribution of the CB aggregate in Chapter 3.

AC is a method of deriving the hydrodynamic parameters of a particle as it moves through a fluid medium in which it is suspended. The hydrodynamic behavior is determined by the mass, density and shape of the particle, and temperature control during the measurement is critical for a successful AC result. 142-143

Particle Sedimentation

The sedimentation speed of particles depends on their size, density and shape. Initially, the dispersion of particles is filled in the sample cuvette. Centrifugation of the sample forces the particles to move from the meniscus to the bottom of the sample cuvette. The intensity of the transmitted light is detected by the charged-coupled device (CCD) sensor across the entire sample and the first extinction profile is recorded. This process is monitored in real time by transmission measurements. The intensity of the transmitted light detected by the CCD sensor increases over time as the particles move from the meniscus to the bottom, allowing more of the incident light to pass through the sample cuvette. The sedimentation behavior and the concentration of particles can be determined from the measured extinction profiles.

The concept of Stokes diameter is one of the key assumptions of AC. The Stokes law describes the rate of motion of a spherical particle with diameter d and density ρ_{NP}, in a fluid with density ρ_s and viscosity η_s[143-144]

$$d = \sqrt{\frac{18\eta_s s}{\rho_{NP} - \rho_s}} \tag{2.5}$$

In equation (2.5), s is the sedimentation coefficient, which normalizes the sedimentation velocity u by the centrifugal acceleration $\omega^2 r$.

$$s = \frac{u}{\omega^2 r} \tag{2.6}$$

The unit of sedimentation coefficient is *Svedberg*, which is 10^{-13} s.

For suspensions with broad particle size distributions or for multimodal colloids, the distribution of sedimentation coefficient distribution $g(s)$ is preferred to the mean sedimentation coefficient for accurate data analysis.

$$g(s) = \frac{\mathrm{d}\left(\frac{c(s)}{c_0}\right)}{\mathrm{d}s} \cdot \frac{r}{r_m}^2 \tag{2.7}$$

where $c(s)$ is the sample concentration for a given sedimentation coefficient, c_0 is the initial sample concentration, s is the sedimentation coefficient, r is the radius from center of rotation and r_m is the meniscus position. The function $g(s)$

gives the concentration $\mathrm{d}m = \mathrm{d}c/c_0$ of the sample sedimenting with a sedimentation coefficient between s and $s + \mathrm{d}s$.

Particle Size Distribution

The basis of particle size distribution (PSD) measurement is the determination of the sedimentation coefficient distribution $g(s)$ of samples.[143, 145] For a polydisperse sample, each fraction of particles has a diameter $d_{p,i}$ and a concentration $c_{0,i}$. The individual particle fractions are assumed to sediment completely, independently of each other, without any mutual interference. For free sedimentation in a laminar regime, the particle size $d_{p,i}$ can be determined for spherical particles using the modified Stokes law.

$$d_{p,i} = \sqrt{\frac{18\eta_s}{(\rho_{NP} - \rho_s)\omega^2 t_m} \ln\left(\frac{r_m}{r_0}\right)} \tag{2.8}$$

where ρ_{NP} is the particle density, ρ_s is the fluid density, η_s is the dynamic viscosity, r_0 is the starting position of the particles, r_m is the measurement position, $\ln\left(\frac{r_m}{r_0}\right)$ is the sedimentation coefficient of the ith fraction of particle and t_m is the measurement time.[146-147]

The mass fraction $m_i = c_{0,i}/c_0$ of each species can be extracted from the measured light intensity values $I(t)$ by the Mie theory[148]. The concentration $c_{0,i}$ can be determined by

$$c_{0,i} = \frac{\ln\frac{I_i}{I_{i-1}} - 2a(t_i - t_{i-1}) \cdot \sum_{n=i+1}^{n=z} \left(\frac{\tau}{c}\right)_n \cdot c_{0,n} \cdot k_n}{a\left(\frac{\tau}{c}\right)_i \cdot \exp(-2 \cdot k_i \cdot t_{i-1})} \tag{2.9}$$

where $t_i - t_{i-1}$ is the time interval, I_i is the light intensity corresponding to time t_i, k_i is the constant of the thinning effect of the ith fraction and $\left(\frac{\tau}{c}\right)_i$ is the specific turbidities, which can be calculated by using the diameter $d_{p,i}$ and the refractive index n_p of the particles. The $c_{0,i}$ values can then yield the relative mass fraction m_i, and the PSD curve can be plotted.

2.3 Electrical Conductivity

This section introduces the basics of electrical conductivity and the measurement methods that will be used to determine the conductivity of PDMS-CB composites in Chapter 3 and Chapter 4.

Electrical conductivity (σ) is a physical property that quantifies the ease with which electric currents pass through a medium when an electric field is applied. The major techniques for measuring the electrical conductivity of composites are the two-point probe and four-point probe methods.

The two-point probe method is based on the definition of resistance according to Ohm's law, i.e. $V = IR$, where V, I and R are the voltage, current and resistance between the two electrodes, respectively. The conductivity of the composite sample can be calculated from the following equation.

$$\sigma = \frac{1}{R} \times \frac{L}{A} \tag{2.10}$$

where L and A are the length and cross-sectional area of the samples, respectively. Because the measured composite sample is usually orthotropic, the conductivities in the other two directions might be different and can be measured similarly.[149]

The measured resistance R should be understood carefully. In fact, the measured resistance R using the two-probe method is the sum of the sample resistance R_0 between the two electrodes, the resistance R_e of electrodes and wires, the resistance R_m of the machine and the contact resistance R_c between the electrodes and the composite sample, as shown in Figure 2.2. The measured resistance R can be approximated to the sample's resistance R_0, only if the sum of the other three resistances is much smaller than the sample resistance R_0. However, contact resistance may be introduced due to imperfect bonding between the electrodes and the composite samples. Since the contact resistance is unknown and difficult to determine, and in some cases, it may be higher than the true resistance of the sample due to poor contact, the two-point probe method is generally not recommended.[150]

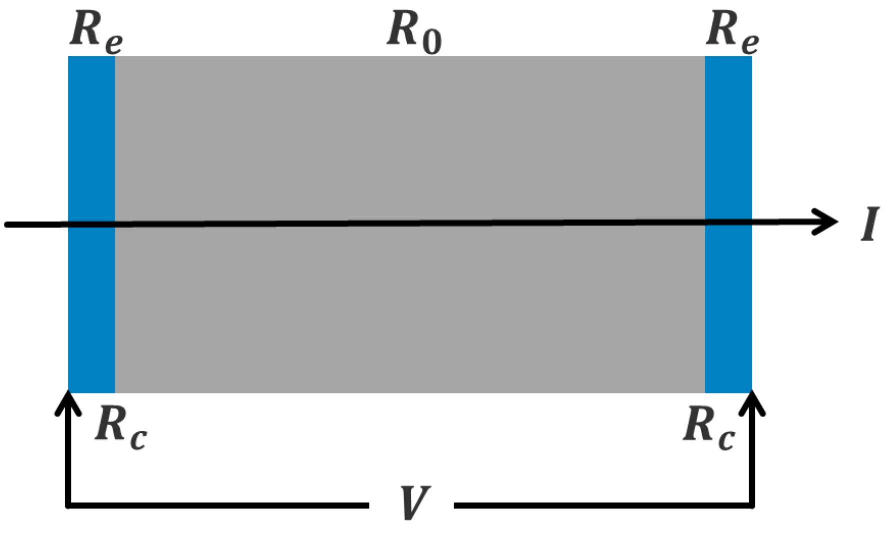

Figure 2.2. Schematic of the two-probe method of conductivity measurement.

The four-point probe method was developed to avoid the errors caused by the contact resistance between the pins and the samples.[150-151] The general four-point probe measurement model is shown in Figure 2.3. Typically, a constant current (I) is applied between the probes 1 and 4, and the voltage (V) between the probes 2 and 3 is measured with a high-impedance voltmeter.

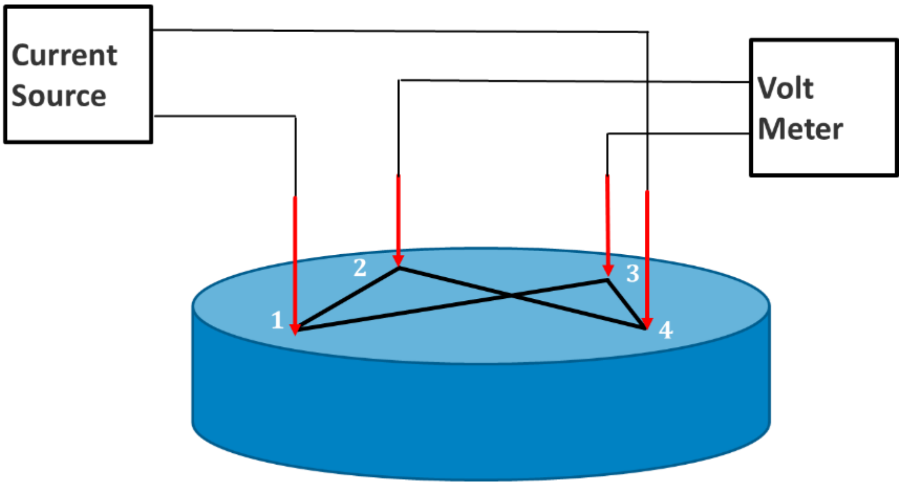

Figure 2.3. Schematic of the general four-point probe measurement method.

The conductivity can be expressed as

$$\sigma = \frac{I}{2\pi \cdot V}\left(\frac{1}{r_{12}} - \frac{1}{r_{24}} - \frac{1}{r_{13}} + \frac{1}{r_{34}}\right) \tag{2.11}$$

where r is the distance between the two probes.

If a collinear type four-point probe method is used, as shown in Figure 2.4, where $r_{12} = r_{23} = r_{34} = S$, then the conductivity calculation can be simplified to

$$\sigma = \frac{I}{2\pi S \cdot V} \tag{2.12}$$

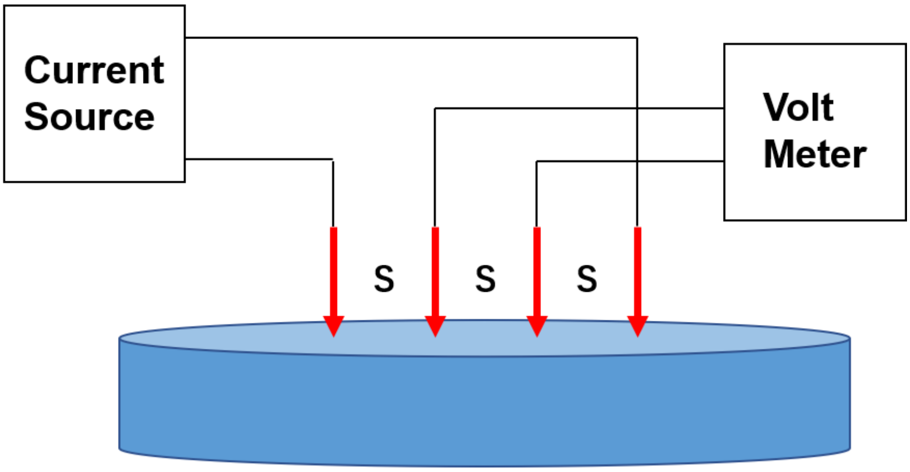

Figure 2.4. Schematic of the collinear four-point probe measurement model.

Typically, the thickness and minimum distance between the pin and the edge of the sample should be at least four times longer than the spacing between two pins (S). Otherwise, if the sample is not semi-infinite, a geometric correction factor B[152] should be introduced to equation (2.12).

$$\sigma = \frac{IB}{2\pi S \cdot V} \tag{2.13}$$

2.4 Small-Angle X-ray Scattering

Small-angle X-ray scattering (SAXS) measurements are performed in Chapter 3 to analyze the structures of CB primary particles, aggregates, and agglomerates in the PDMS matrix.

SAXS is a method for characterizing the structural properties of nanomaterials. SAXS analyzes the intensity of X-rays scattered by a material as a function of the scattering angle in a narrow-angle window between 0.1 and 5 degrees. Solids, powders, gels, and liquid dispersions are all possible samples, and they can be amorphous, crystalline, or semicrystalline. Measurements require only a small amount of sample. Ultra-small-angle X-ray scattering (USAXS) with longer sample-detector distance (SDD) can distinguish even larger dimensions, because the smaller the angle recorded, the larger the dimensions of the analyzed object.

Structure Factor and Form Factor

SAXS can be used to evaluate particle shape or size distribution. The intensity pattern of a single particle can be extrapolated from the obtained SAXS patterns. To obtain the intensity pattern of a single particle, it is necessary to eliminate the concentration effect, which appears as a peak in the intensity patterns due to the proximity of neighboring particles. The peak comes from the structure of the solution, and the average particle distance is roughly $2\pi/q^*$, where q^* is the position of the peak. The intensity of SAXS can be written as:

$$I(q) = P(q) \times S(q) \tag{2.14}$$

where $I(q)$is the intensity as a function of the scattering vector q, $P(q)$is the form factor, which characterizes the scattering from a single particle in a dilute solution and depends significantly on its size and shape, and $S(q)$ is the structure factor, which is a function of the arrangement of the particles in the solution.

In dilute systems, $S(q)$ can be assumed to be 1, because the particles are free to move everywhere in the solution. When particle concentration in solution becomes high enough, the concentration effect cannot be ignored in the scattering curves. As the concentration of particles begins to increase, the particles are more likely to be closer. This gives rise to a maximum in the structure factor and at smaller q values $S(q)$ starts to get lower.[153]

Guinier Regime

Guinier approximation can be used to determine the radius of gyration (R_g) of the particles. Guinier approximation is valid for particles at low concentrations and in the low q value range, where diffraction is insensitive to details of the particle structure. The Guinier approximation equation can be expressed as

$$I(q) = I_0 \exp\,[-\frac{1}{3}\left(qR_g\right)^2] \tag{2.15}$$

The slope of a plot of $ln[I(q)]$ $vs.$ q^2 directly describes the radius of gyration of the scattering particles. The radius of gyration is not sufficient to determine the actual shape of the particle, because the interpretation assumes that the particles are spherical. However, with particles of known shape, the radius of gyration can be used for calculating the size of the particles.[153-154]

Porod Regime

Günther Porod discovered Porod's law in 1951, which is used to interpret scattering intensities at large q values. According to Porod's law, the slope of the plot represents the surface fractal dimension of the scattering objects.[154] A slope of -2 is common for a polymer chain in a dilute solution at high q, while stiff rod-like molecules have a slope of -1. A spherical particle with a smooth surface has a slope of -4, and a slope between -3 and -4 represents a rough surface.

Scattering of Fractal Objects

Hierarchical structures (for example, in CB there is a three-hierarchical structure, namely a primary particle, an aggregate and an agglomerate) can be studied using SAXS. For a hierarchical structure dispersed in a medium, the scattering intensity can be expressed as

$$I(q) = \varphi V < \Delta\rho >^2 P(q)S(q) \tag{2.16}$$

where $P(q)$ is the form factor, $S(q)$ is the structure factor, V is the particle volume, φ is the overall filler volume fraction and $< \Delta\rho >^2$ is the scattering contrast between the matrix and the filler.

Under dilute conditions, $S(q)$ can be assumed as 1, and equation (2.16) is reduced to

$$\frac{I_0(q)}{\varphi_0} = V < \Delta\rho >^2 P(q) \tag{2.17}$$

To describe the multiscale structural hierarchies, the dilute reduced scattering intensity in equation (2.17) can be determined from the unified scattering function and expressed as

$$\frac{I_0(q)}{\varphi_0} = \sum_{i=1}^{n} \left[G_i \exp\left(\frac{-q^2 R_{g,i}^2}{3}\right) + B_i (q_i^*)^{-P_i} \exp\left(\frac{-q^2 R_{g,i-1}^2}{3}\right) \right] \tag{2.18}$$

where "i" is the structure level, G_i and B_i are the Guinier and Porod pre-factors that account for the particle volume V, respectively, and $< \Delta\rho >^2$ is the scattering contract, $R_{g,i}$ is the radius of gyration, which specifies the size of structural level in the hierarchy; the power-law exponent P_i specifies the morphology of each structural level and varies between 1 and <3 for mass-fractal objects.

In equation (2.18),

$$q_i^* = q\left[\operatorname{erf}\left(\frac{kqR_{g,i}}{\sqrt{6}}\right)\right]^{-3} \tag{2.19}$$

where "erf " is the error function, and k equals 1 for three-dimensional structures and approximately 1.06 for mass-fractal structures.[155-156] The unified approach can distinguish Guinier regimes buried between two power-law regimes. It is applicable to a wide variety of systems.[157-158]

Equation (2.18) was used in this dissertation to fit the scattering curves and derive the fractal dimensions.

2.5 Swelling

Swelling experiments are performed to analyze the PDMS matrix change caused by ionic liquid (IL) in Chapter 4.

Polymer swelling theory was defined by Flory and Rehner who assumed that the change in free energy of a swollen polymer system is composed of contributions due to mixing of the polymer and solvent, and elastic deformation of the network strands.[159] The mixing of polymer and solvent can be described by the Flory-Huggins theory[160-161], and the elastic deformation of the network is described by the affine network model[162]. The swelling method is commonly used to determine network parameters such as cross-linking density.

The swelling capacity of the polymer can be quantified by the mass swelling ratio D_{sw} or the volume swelling ratio D, defined as follows:

$$D_{\mathrm{sw}} = \frac{m_{\mathrm{sw}} - m_{\mathrm{dy}}}{m_{\mathrm{dy}}} \times 100\% = \frac{m_{\mathrm{st}}}{m_{\mathrm{pr}}} \times 100\% \tag{2.20}$$

$$D = \frac{V_{\mathrm{sw}}}{V_{\mathrm{dy}}} \times 100\% = \frac{V_{\mathrm{st}} + V_{\mathrm{pr}}}{V_{\mathrm{pr}}} \times 100\% = \left(1 + D_{\mathrm{sw}} \times \frac{\rho_{\mathrm{pr}}}{\rho_{\mathrm{st}}}\right) \times 100\% \tag{2.21}$$

where m_{sw} and m_{dy} are the weights of the sample in the swollen and dry states respectively, V_{sw} and V_{dy} are the corresponding volumes. m_{st} and m_{pr} are the masses of the solvent and the polymer, respectively, V_{st} and V_{pr} their volumes and ρ_{st} and ρ_{pr} their densities.[163]

2.6 Stress-Strain Behaviors of Elastomers

Filler particles improve the tensile strength, tear resistance and abrasion resistance of the elastomer. Tensile test has been widely used to investigate the mechanical properties of elastomer composites.[164-166] In Chapter 4, tensile tests are performed to determine the Young's modulus and elongation at break of the composites.

Figure 2.5 shows typical strain-stress relations for pure elastomer, low filler load and high filler load elastomer composites. Elastomer composites become stiffer and less flexible as filler loading increases.

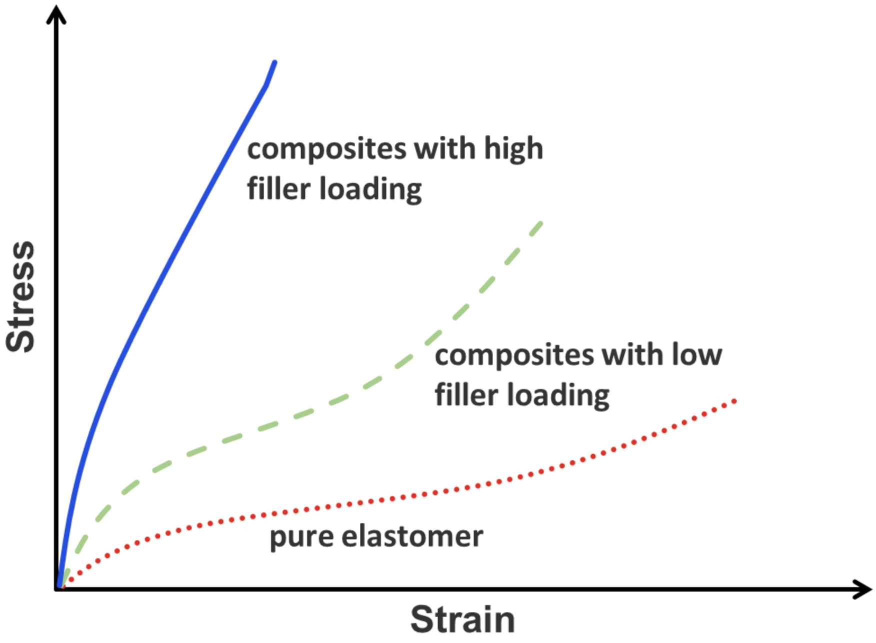

Figure 2.5. Examples of stress–strain relations of the pure elastomer, elastomer composites with low and high filler loadings.

Young's modulus describes the elastic properties of a solid under tension or compression in one direction, as in the case of a solid that returns to its original length after being stretched or compressed longitudinally.[167] For example, as shown in Figure 2.6, when an object is in tension, a force $\vec{F}$ is applied to the surface area A, the object is elongated by Δl from its original length l_0. The Young's modulus (E) can be expressed as

$$E = \frac{tensile\ stress}{tensile\ strain} = \frac{|\vec{F}|}{A} \times \frac{l_0}{\Delta l} \tag{2.22}$$

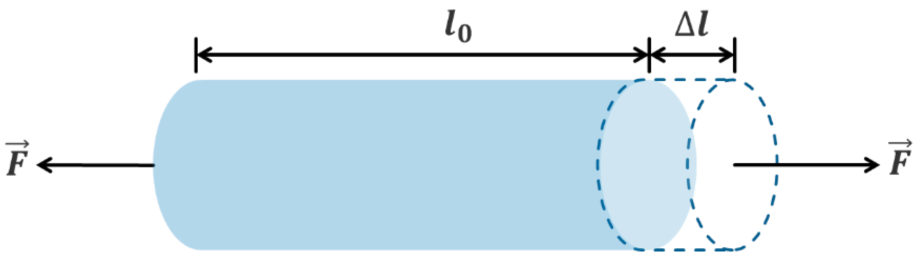

Figure 2.6. Object under tension in the range of elastic deformation.

2.7 Rheology

To understand the interactions between PDMS, CB, and IL, rheological measurements are performed in Chapter 4.

The rheology of dispersed systems is a critical property for characterizing the flow behavior of dispersions. The rheological properties of dispersions are complex and highly dependent on the applied forces, especially at high solid concentrations. Viscosity is a measure of a fluid's resistance to flow. Adding filler particles usually increases the viscosity of the fluid, and this is also a major reason why the Newtonian behavior of a fluid changes.[168-169]

Viscosity, Shear Stress, Shear Rate and Modulus

The concept of viscosity (η) was first introduced by Isaac Newton as a proportionality constant between the force per unit area (shear stress, τ) required to produce a steady, simple shear flow and the resulting velocity gradient in the flow direction (shear rate, $\dot{\gamma}$)

$$\tau = \eta\dot{\gamma} \tag{2.23}$$

Different materials have different shear stress and shear rate relations. Newtonian fluid exhibits a linear relationship between shear stress and shear rate, and viscosity in Newtonian fluid is thus independent of shear stress, shear rate and time. Bingham fluid requires a minimum shear stress to deform the fluid. Materials such as dispersions, emulsions, their viscosities decrease or increase with increasing shear rate, are cataloged as shear thinning and shear thickening fluids.[168] Figure 2.7 describes the comparison of the fundamental change of the Newtonian, Bingham, shear-thinning, and shear thickening behavior in shear stress and viscosity as a function of shear rate.

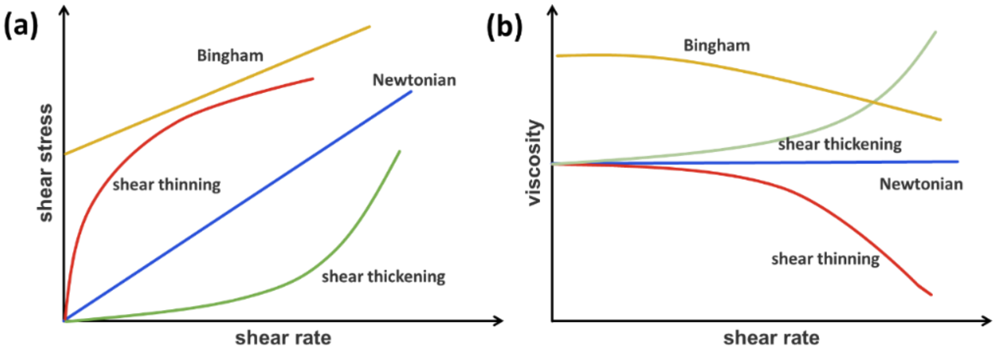

Figure 2.7. Typical flow curves for Newtonian, Bingham, shear-thinning and shear thickening fluids, (a) shear stress as a function of shear rate, (b) viscosity as a function of shear rate.

Many materials exhibit viscoelastic behavior (a mixture of viscous and elastic behavior) when sheared, and small-amplitude oscillatory shear tests are often used to derive the rheological properties of materials.[170] For the viscoelastic materials, when a sample is strained at small strain amplitudes, the shear stress will be a sine wave of the same frequency as the input strain wave. However, the shear stress will have a phase difference (δ) with the input strain. The complex shear modulus G^* can be written as

$$G^* = \frac{\tau_0}{\gamma_0} \tag{2.24}$$

where τ_0 is the shear stress amplitude and γ_0 is the strain amplitude.

The storage modulus ($G' = G^* \cos\delta$) represents the elastic portion of the viscoelastic behavior, and partially describes the solid-state behavior of the sample. The elastic portion of the energy is stored in the deformed material by properly stretching and elongating the internal structures to prevent overstressing the interactions and destroying the materials. When the material is released after deformation, the unused stored energy acts as a driving force to return the structure to its original shape. The loss modulus ($G'' = G^* \sin\delta$) characterizes the viscous part of the viscoelastic behavior, which can be considered as the liquid state behavior of the sample and characterizes the deformation energy lost due to internal friction during flow or deformation.[170]

Rheometer and Test Geometries

The rheometer is the basic experimental instrument for determining the flow properties of fluids. In this dissertation, rotational rheometers were used to derive viscosities, storage and loss moduli. In rotational rheometers, the shear is added between stationary and moving solid surfaces.[168] The flow properties of materials can be measured with rotational rheometers in a steady, simple shear flow with a homogeneous deformation regime. Constant speed or constant torque can be used to determine shear rate and shear stress. Some of the rotational rheometers can be used to measure viscoelastic material properties using the harmonic oscillation function. The concentric cylinder, cone-and-plate, and parallel plate measurement systems are the most commonly used geometries in current rotational rheometers, as shown in Figure 2.8.[168]

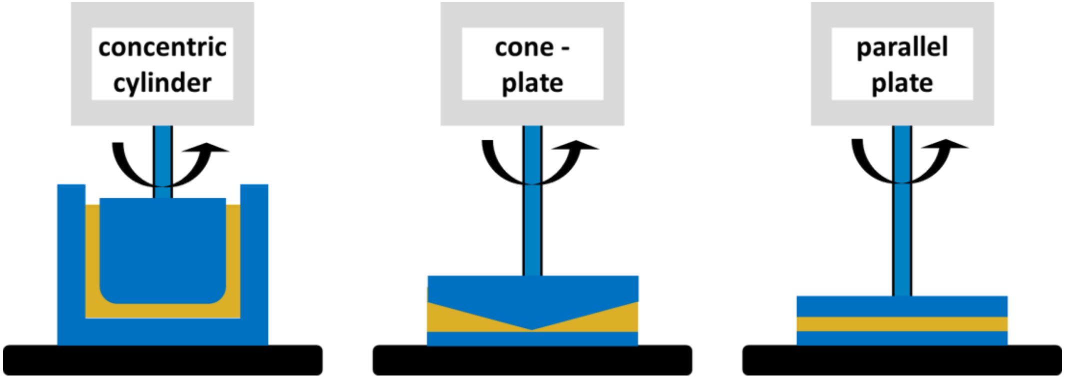

Figure 2.8. Schematic of (a) concentric cylinder, (b) cone-plate, and (c) parallel plate geometries for the rotational rheometer.

The concentric cylinder geometry is the most convenient and suitable for low viscosity liquids, because it provides a large shear area and at high shear rates the sample is not expelled from the gap. The concentric cylinder geometry has a high surface area contact with the samples and minimal sample evaporation, but the shear rate is not uniform across the gap. The cone-plate geometry provides a uniform shear rate across the gap and is therefore the most accurate test geometry. The use of the cone-plate geometry is limited by factors such as the limited maximum particle size of the sample, difficulties in avoiding solvent evaporation, temperature gradients in the sample and concentration gradients due to sedimentation. The parallel plate geometry allows the gap width to be varied, and the parallel plate geometry allows the measurement of suspensions with large particles by using large gap heights. On the other hand, by operating with small gaps, viscosity can be obtained at relatively high shear rates. However, as with the concentric cylinder geometry, the shear rate is not uniform across the gap.

3 Percolation and Fractal Dimension of Carbon Black Aggregates in PDMS Matrix[*]

This chapter presents the results of tuning the electrical properties of PDMS-CB composites from the perspective of the CB fillers. The effect of CB aggregate size on the conductivity of PDMS-CB composites was investigated. To test the hypothesis that the aggregate size affects the conductive network structure and the conductivity of the composite, ball-milling was used to tune the CB size, and the unground and ball-milled CB were used to prepare the composites. To further investigate the structures of the CB fillers in the composites, the PDMS-CB composites were measured using ultra-small-angle X-ray scattering (USAXS). The fractal dimensions of primary particles, aggregates and agglomerates were derived from the scattering curves. By comparing the scattering curves of different CB loadings, the agglomeration of CB aggregates in the PDMS matrix was discussed. Finally, an attempt was made to correlate the conductivity changes with the structure formation of the CB network in the PDMS matrix.

3.1 Experimental Section

Materials

Carbon black (carbon black, acetylene, 100% compressed, 99.9+ %, bulk density 170-230 g/L, Alfa Aesar, product number 45527), PDMS (SYLGARD™ 184 Silicone Elastomer Kit), isopropanol (≥99.7%, Sigma-Aldrich), and toluene (toluene anhydrous, 99.8 %, Sigma-Aldrich) were used as received without further processing.

---

[*] The data has been published in the article “Percolation of rigid fractal carbon black aggregates”, *J. Chem. Phys.*, **2021**, 155, 124902, and the text has been rewritten to fit the structure of the dissertation.

Ball-Milling

Planetary ball-milling experiments were performed to investigate the relationship between filler size and composite conductivity. For all experiments, 1.5 g of CB powders were placed in a 50 mL zirconia (ZrO_2) grinding jar with 30 mL isopropanol, and ball-milled at 400 rpm for 2 hours, with direction reversal every 10 min. 60 g and 120 g ZrO_2 balls (1 mm in diameter) were used, to acquire two different CB size distributions. The as prepared CB powders were named ball-milled CB-1 and ball-milled CB-2, respectively. The ball-milled CB powders were washed with isopropanol and centrifuged, and then dried at 100 °C overnight. The dried CB powders were collected for further use.

Size Distribution Characterization

The size distribution of the CB was analyzed by analytical centrifugation (AC) using a LUMiSizer 651 (LUM GmbH, Berlin, Germany). 0.0014 wt-% CB/toluene suspensions were prepared by ultrasonication for 30 min in an ultrasonic bath (Elmasonic S 100H). AC test was performed immediately after filling the polyamide (PA) cells with 430 µL suspensions, and transmission was measured at a blue wavelength of 470 nm and a temperature of 20 °C for all tests.[171]. Particle size distributions were analyzed using SEPView software with a volume-weighted particle size distribution function.

Composites Preparation

The composites were prepared by mixing CB fillers and PDMS in different volume ratios in a Speedmixer (DAC 600.2 VAC-P Vacuum Mixer System). First, CB powders and PDMS base were mixed at 2350 rpm under vacuum for 3 minutes. Second, the curing agent was added to the PDMS-CB mixture, and the mixture was remixed under the same conditions. The mass ratio of curing agent to PDMS is 1:10. The mixture was cured at 100°C for 2 hours.

Conductivity Measurement

The electrical conductivity of cured bulk samples was measured using the four-probe method with a source meter Keithley 2450 (Tektronix, Inc., USA) at room temperature. Voltage values were recorded as the current varied from -10^{-5} to 10^{-5} A in 200 steps, and a linear fit of the current-voltage curve was used to derive the resistance. The conductivity of the composites was calculated using equation (2.12).

Ultra-Small-Angle X-ray Scattering

The ultra-small-angle X-ray scattering (USAXS) experiment in transmission geometry was carried out at the P03/MiNaXS beamline at the synchrotron source PETRA III at Deutsches Elektronen-Synchrotron (DESY), Hamburg, Germany.[172] The experiments were performed during two campaigns: One used an X-ray beam with an energy of 12.85 keV (wavelength λ=0.0965 nm, $\Delta\lambda/\lambda = 10^{-4}$) and the second 11.8 keV with a wavelength of λ=0.105 nm. In both cases, the X-ray beam was focused on the detector by beryllium compound refractive lenses (CRL) with the sample-detector distance (SDD) = 9760 mm and 9348 mm, respectively. Transmission was measured by a diode inside the beamstop. The beamstop was deliberately shifted away from the transmitted X-ray direct beam[173] to reach ultra-small scattering angle. A PILATUS 300K detector (Dectris Ltd., Switzerland) with pixel size of 172×172 μm^2 and 487×619 square pixels (83.8×106.5 mm^2) was used as an area detector. Azimuthally averaged radial distributions of intensity were calculated after the analysis of the USAXS data using the DPDAK software package.[174]

Other Characterization Methods

Transmission electron microscopy (TEM) images were recorded using a JEM-2010 (JEOL, Germany), working at 200 kV. Surface adsorption measurement was performed with Quadrasorb EVO (Anton-Paar, Austria), measured at 77.35 K using 0.0613 g CB powders. It was heated up to 130 °C and degassed under vacuum for 10 hours. After cooling, the sample weight was determined, the filler rod was inserted into the sample cell, and then the sample cell was placed in the measuring instrument.

3.2 Results and Discussion

Figure 3.1 shows the TEM image of CB used in this work, and the primary particle diameters are mostly distributed in the range of 32 to 48 nm.

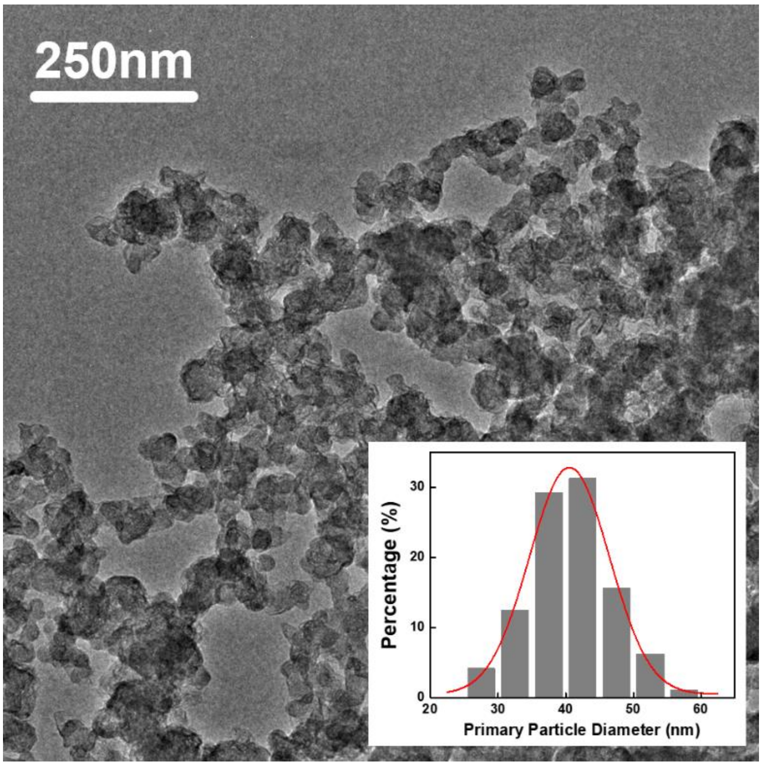

Figure 3.1. TEM image and primary particle size distribution histogram of CB.

Nitrogen adsorption measurement was performed to measure the SSA of CB powders. The SSA was determined to be 76.549 m²/g, which is close to the manufacturer's claim of 75 m²/g. The fractal dimension of CB powders was calculated using equation (2.4). As shown in Figure 3.2, V and V_0 represent the volume adsorbed at pressure P and on the monolayer, respectively, and P/P_0 is the partial pressure. The slope of -0.43 indicates a fractal dimension of 2.57

according to equation (2.4), which is similar to the fractal dimension value of 2.5 of a theoretically studied 3D DLA cluster.[50, 175]

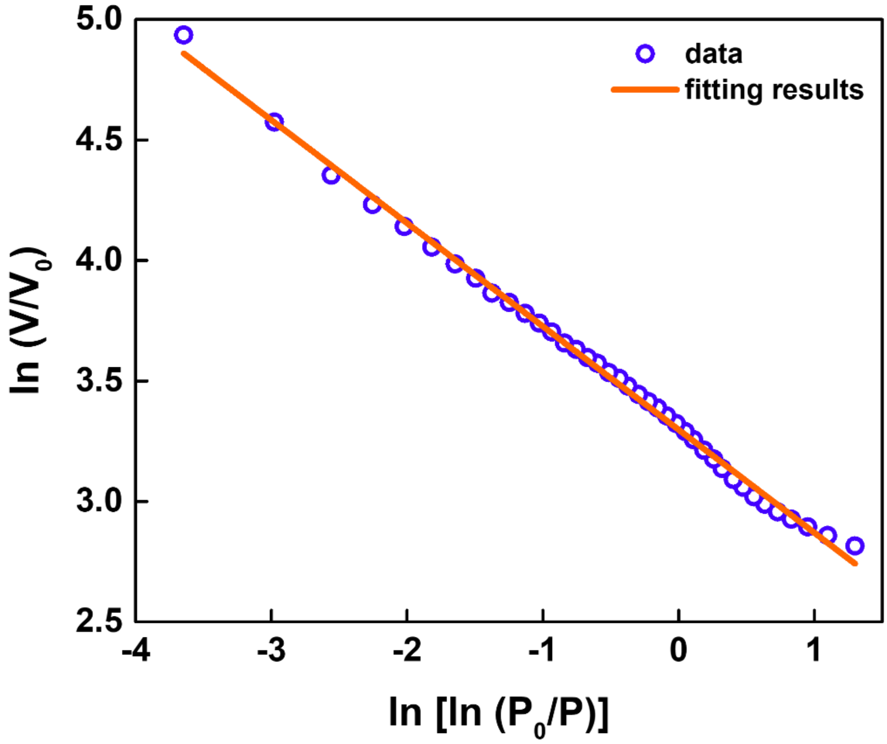

Figure 3.2. Frenkel–Halsey–Hill (FHH) plot of the adsorption branch of the nitrogen adsorption-desorption isotherms of CB powders.

For the ball-milling experiments, the ball-milling time was fixed, and the ball-milling intensity was varied by changing the number of collisions, i.e., changing the number of ZrO_2 balls. And AC was used to determine the size distribution of unground CB and ball-milled CB dispersed in toluene. As shown in Figure 3.3, the unground CB aggregates range in size from 60 to 800 nm, as indicated by the distribution curve colored in blue. The distribution range remains similar for ball-milled CB-1 and CB-2, as shown by the distribution curves colored in green and red, respectively. However, there is a clear shift of the peak to a smaller value, from 324 to 237 nm, indicating that the proportion of smaller aggregates increases with increasing ball-milling intensity. The AC result shows that ball-milling broke the large aggregates into smaller segments and changed the overall size distribution. The aforementioned CB primary particle size, SSA, fractal dimension and aggregate size distribution provide the basic "picture" of the CB fillers, and the information was also used to build models to simulate the percolation behavior of fractal materials, which were published with Coupette and others.[176] For detailed simulation results, readers are referred to our publication entitled "Percolation of rigid fractal carbon black aggregates".

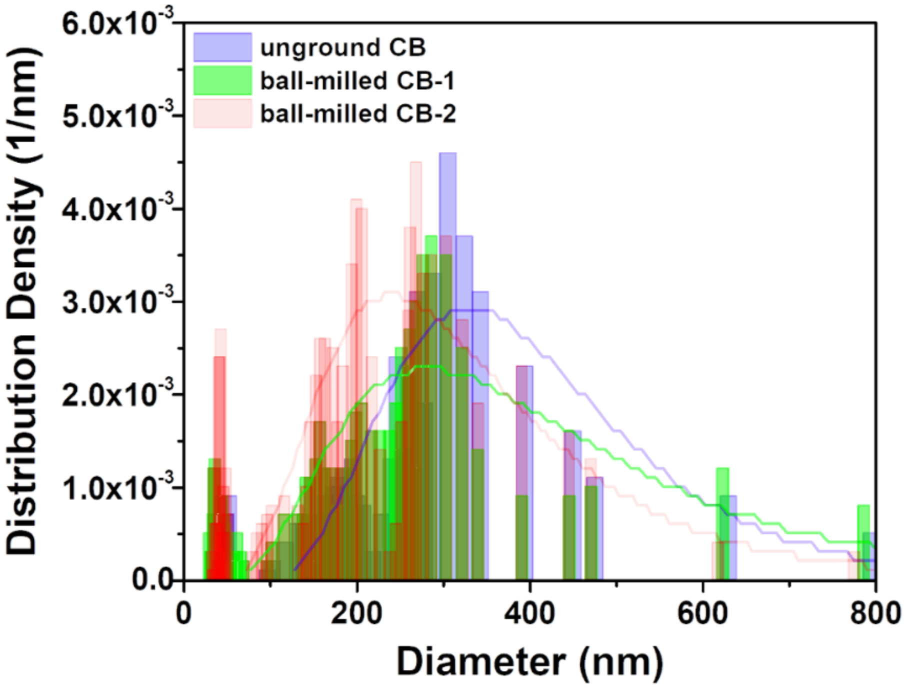

Figure 3.3. Size distributions of unground CB and ball-milled CB dispersed in toluene from analytical centrifugation.

In industrial elastomer-CB composites, multiple components are often used, produced at different temperatures, and subjected to multiple chemical processes. To simplify the conductive networks formed by CB and to limit other components that could affect agglomeration, elastomer composites containing only PDMS and CB were investigated in this chapter. Both unground and ball-milled CB powders were used to prepare the PDMS composites to study the effect of filler size on conductivity. The conductivities of the PDMS composites were measured using the four-point probe method and the percolation thresholds were derived using equation (1.5). As shown in Figure 3.4, the conductivity of the PDMS composite increased with the CB volume fraction for each CB set. The three data sets were fit separately, and the percolation thresholds were determined to be 4.52, 6.96 and 7.76 vol-% for the unground CB, ball-milled CB-1 and ball-milled CB-2, respectively.

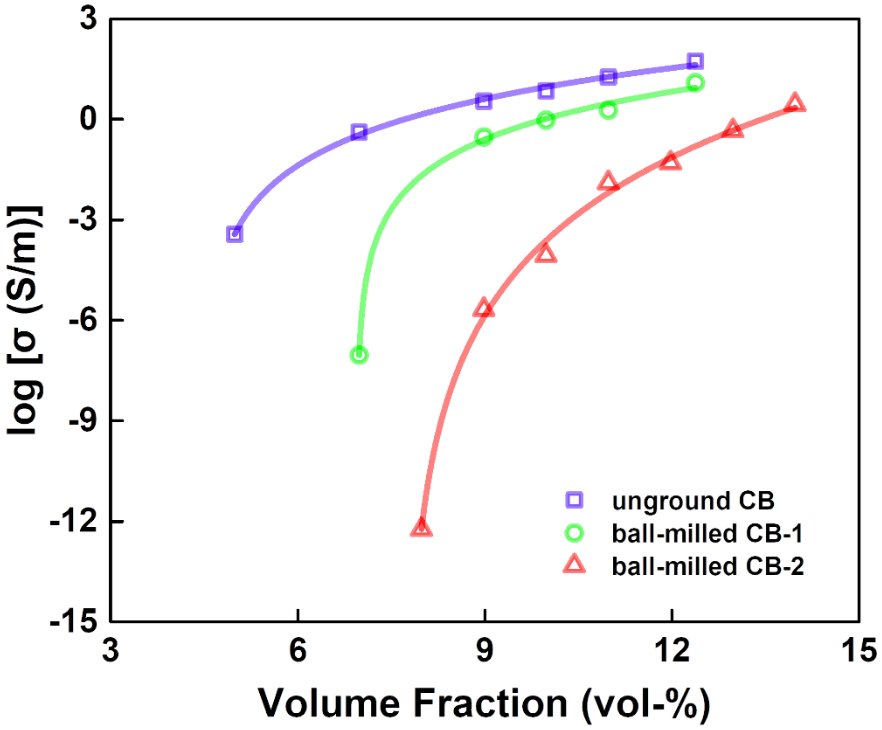

Figure 3.4. Measured electrical conductivities as a function of CB volume fraction for unground and ball-milled CB filled composites. Percolation thresholds are 4.52, 6.96 and 7.76 vol-% for unground CB, ball-milled CB-1 and ball-milled CB-2 filled composites, respectively.

Figure 3.3 and 3.4 show that ball-milling increased the percolation threshold. This result means that the proportion of large aggregates plays an important role in determining the conductivity of as-prepared PDMS composites. As ball-milling intensity increases, the proportion of small aggregates increases, and smaller aggregates may tend to agglomerate into more tightly packed clusters during mixing, requiring more filler to reach the percolation threshold. This explanation is also consistent with the findings of Medalia and co-workers.[177] Figure 3.4 also shows that ball-milling decreased the total conductivity for composites with the same filler concentrations. And the decrease in conductivity for composites with the same filler concentration could be a result of the decrease in the number of conductive paths, as the smaller aggregates are more difficult to disperse separately in the PDMS matrix to form more conductive paths.

Our collaborators have used Monte Carlo simulation to study the percolation of fractal aggregates.[176] Simulation results show that percolation thresholds coincide if they are expressed as a function of the ensemble averaged radius of gyration of the aggregates. Higher order moments of the size distribution had no effect on the percolation threshold; however, aggregates with larger average sizes reduced the percolation threshold. A similar discovery was achieved in a study of fracture networks,[178] in which the percolation of two-dimensional polygons in three-dimensional space was simulated. The experimental results are in agreement with the simulations performed by our collaborators, demonstrating that even for a filler system as complex as CB, systematic studies comparing experiment and simulation can be performed.

To further understand the difference in the conductive network formation of the unground and ball-milled CB, a structural study of the hierarchical structure of the unground and ball-milled CB in the PDMS matrix and their fractal dimensions was measured using the synchrotron USAXS at DESY, Hamburg, Germany. The unfilled PDMS background was subtracted to show only the scattered signals from the CB fillers. In Figure 3.5, the dots colored in yellow show the result of CB scattering intensities, derived from PDMS composites containing 1 vol-% unground CB fillers, and the black line refers to the corresponding fit result using equation (2.18). In general, the scattering curve can be divided into three regions, P_1, P_2 and P_3, which roughly correspond to the primary particle, aggregate and agglomerate, respectively. The high-q region P_1 corresponds to the structure of the primary particles. The surface scaling factor of the P_1 region is about -3.21, which is different from -4 (the surface scaling factor of an ideal sphere) and can be explained by the high roughness of the primary particle surface and the CB-elastomer interphase, as proposed by Ehrburger-Dolle and co-workers.[61-62, 179-180] The mid-q region P_2 and the low-q region P_3 are often explained as the structure of aggregates and agglomerates, respectively. For the mid-q region P_2, the scaling factor derived using equation (2.18) shows a value of -3.16, which means that the fractal dimension is not in the range of the mass fractal dimension from 1 to 3. Considering the broad size distribution of CB aggregates as indicated by the AC experiment, it can be inferred that in the region P_2, the fractal dimension is the governed by both CB aggregates and CB agglomerates of the similar sizes, resulting in a scaling factor of -3.16, which is different from the mass fractal scattering scaling factor reported by Salome[181] and Jäger[137].

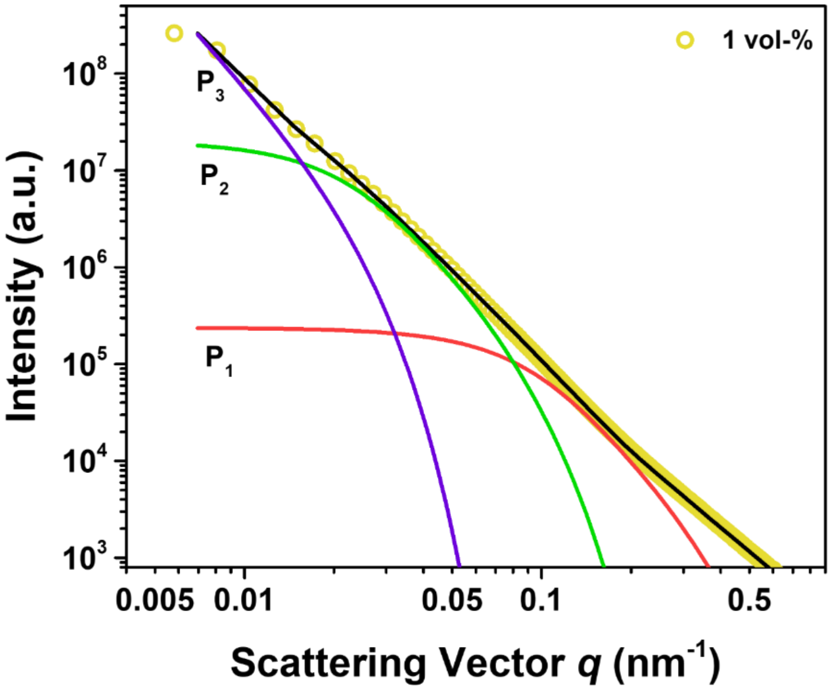

Figure 3.5. Measured CB scattering intensity (yellow dots) extracted from the PDMS composites with 1 vol-% unground CB and its fit (black line).

Composites with different unground CB loadings were tested and the CB scattering signals were extracted. The scattering intensities plotted in Figure 3.6 have been multiplied by the cubed scattering vector q. This plot makes it possible to distinguish the transition of different hierarchical levels of carbon sheets, primary particles and aggregates/agglomerates in the q ranges above 0.18 nm^{-1}, between 0.18 nm^{-1} and 0.044 nm^{-1}, and below 0.044 nm^{-1}, respectively. The q region with negative slope indicates that the scattering is primarily from the surface fractal of the primary particles. Larger wave vectors correspond to fractal scattering from the carbon sheets that form the individual primary particles, while smaller wave vectors correspond to aggregate/agglomerate fractal scattering. As discussed earlier, although the fitting result can show both aggregate and agglomerate scattering, there is considerable overlap between regions P2 and P3 due to the broad size distribution. As a result, the aggregate and agglomerate scattering cannot be well distinguished in Figure 3.6.

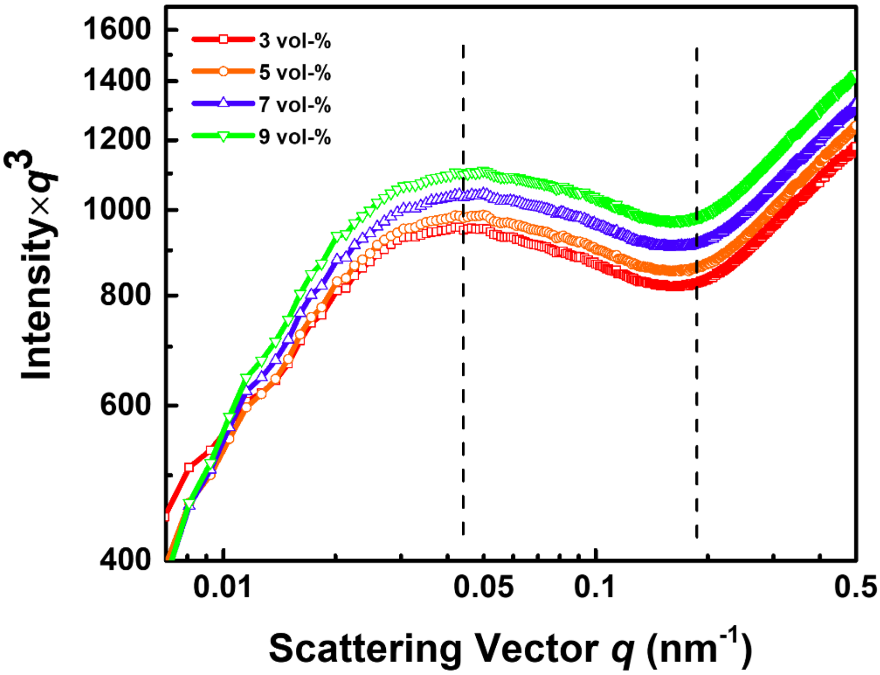

Figure 3.6. Synchrotron USAXS data of composite samples with unground CB fillers. The scattered intensities have been scaled by the cubed scattering vector q to emphasize the different hierarchical levels.

Changing the CB volume fraction did not affect the primary particles, as indicated by the common q position of the maximum and minimum as well as the identical slope in the respective q regions for all CB loadings investigated.

This indicates that the processing did not affect the shape of the primary particles. However, there was a clear slope difference in the largest size range (lowest q values), indicating that agglomerates were formed, and their formation was influenced by the CB volume fraction.

The milling effect was also confirmed by additional USAXS measurements. Composites with different ball-milled CB-2 loadings were tested, and the CB scattering signals were extracted and multiplied by the cubed scattering vector q, as shown in Figure 3.7.

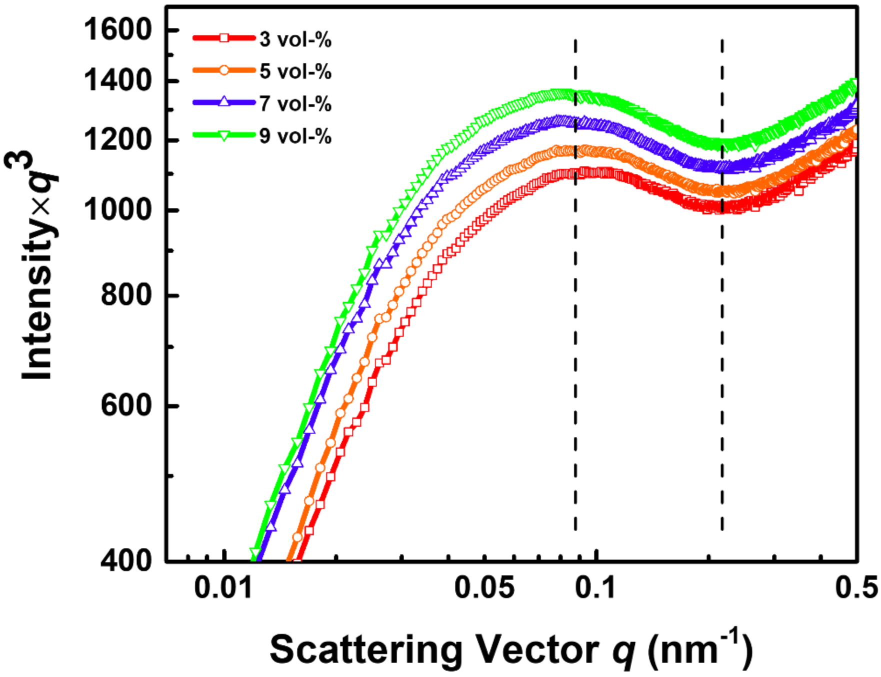

Figure 3.7. Synchrotron USAXS data of composite samples with ball-milled CB-2 fillers. The scattered intensities have been scaled by the cubed scattering vector q to emphasize the different hierarchical levels. Compared to the data shown in Figure 3.6, the curves are shifted to higher q values, indicating smaller structures.

The scattering behavior of samples using ball-milled CB-2 was comparable in the q range for primary particles but significantly different at lower q values. The inflection point changed from 0.044 nm^{-1} to 0.089 nm^{-1}, indicating a change in the size of aggregates and agglomerates. As aggregates become smaller, they compete for the q region previously dominated by primary particles. Thus, the scattering intensity of aggregates generally shifts to higher q values, interfering with primary particle scattering, while reducing intensity at small q. The q region dominated by scattering from aggregates/agglomerates expands towards the direction of smaller q values, confirming the smaller sizes reported from the AC experiment. And for composites with the same concentration of unground and ball-milled CB, the slope in the low q region in Figure 3.7 is steeper than the slope observed in Figure 3.6, indicating that the agglomeration behavior of ball-milled and unground CB in the PDMS matrix is different due to different aggregate size distributions.

Nevertheless, the polydispersity of the aggregates/agglomerates still prevents a comprehensive quantitative analysis of the fractals corresponding to the aggregate and agglomerate levels, respectively. The maximum structural information that can be obtained with the USAXS used in this study is around 900 nm, so no information was provided for agglomerates larger than 900 nm in this analysis.

3.3 Summary

In this chapter, an attempt has been made to study the percolation threshold and the structures of CB fillers in PDMS matrix. TEM was used to determine the diameter of the primary particles. Nitrogen surface adsorption was used to determine the specific surface area and fractal dimension of the CB powders. Ball-milling and AC experiments were performed to confirm the ball-milling effect on the size distributions of the CB aggregates. The conductivities of the PDMS-CB composites were measured by the four-point probe method, and a comparison of percolation thresholds was made to discuss how the size distributions of the CB fillers tune the conductive behavior of the composites.

The fractal dimensions and the ball-milling effect were further confirmed and discussed using USAXS data.

The AC results showed that ball-milling increased the proportion of smaller aggregates and decreased the number of larger aggregates. And the size distribution of the CB aggregate has a significant effect on the percolation threshold, which is confirmed by the conductivity measurements that more ball-milled CB filler was required to reach the percolation threshold compared to the unground CB. And for composites with the same concentration of unground and ball-milled CB, composites with ball-milled CB showed lower conductivity, the possible explanation is that ball-milling increased the proportion of smaller aggregates, which tend to agglomerate into larger clusters, reducing the percolation paths and thus the conductivity. The difference in agglomeration behavior of unground and ball-milled CB in the PDMS matrix caused by the CB aggregate size distributions is also confirmed by the USAXS curves in the lower q value ranges.

By varying the size of the fractal fillers, this conclusion provides the design concept for composites, i.e., a larger aggregate is preferred if one wants to use less filler to make the composite conductive.

4 Microscopic Softening Mechanisms of Ionic Liquid in Conductive PDMS-CB Composite[†]

This chapter presents the results of tuning the electrical and mechanical properties of PDMS-CB composites from an IL perspective. IL as an additive alters the conductive network in the elastomer matrix, and thus influences the electrical and mechanical properties of the composites. In this chapter, how IL [EMIM][TFSI] alters the structures and properties of PDMS-CB composites was investigated. For this purpose, different amounts of IL were added to prepare the PDMS-CB composites. Conductivity was measured using the standard four-point probe method, and mechanical properties of Young's modulus and elongation at break were derived from tensile test results. To further investigate the role of IL in the composite and the interaction of IL with PDMS and CB, swelling, light microscopy and rheological tests were performed on the PDMS-IL and PDMS-IL-CB composites.

4.1 Experimental Section

Sample Preparation

The composites were prepared using commercial PDMS (SYLGARD™ 184 Silicone Elastomer Kit, Dow Inc.) as the polymer matrix and carbon black (45527, acetylene, 100 % compressed, 99.9+ %, Alfa Aesar) as the filler. The volume ratio of CB fillers was fixed at 9 vol-% (14.8 wt-%) in the PDMS-CB mixtures. This CB fraction is larger than the reported percolation threshold of 4.52 vol-% reported in Chapter 3. IL [EMIM][TFSI] (Sigma-Aldrich) was used as an additive.

[†] The results in this chapter have been published in the article "Microscopic Softening Mechanisms of an Ionic Liquid Additive in an Electrically Conductive Carbon-Silicone Composite" *Adv. Mater. Technol.* **2022**, 7, 2101700, and the text has been rewritten to fit the structure of the dissertation.

Different amounts of IL were added to PDMS-CB mixtures, where the mass ratio of IL/CB was 0.19, 0.38, 0.57, 0.77, and 0.96, and the corresponding composites were named as PDMS-CB-IL-1, -2, -3, -4 and -5, respectively. The elastomer composites were prepared in two steps to ensure homogeneous mixing. First, CB fillers, IL, and the PDMS base were mixed in a SpeedMixer (DAC600.2 VAC-P, Hauschild Engineering, Hamm, Germany) at 2350 rpm under vacuum for 3 min. The curing agent was added after mixing all the other components and the mixing step was repeated. The mass ratio of curing agent to PDMS is 1:10. The samples were cured at 100 °C for 2 hours in a cylindrical mixing jar with a diameter of 33 mm, and the solid samples as prepared were measured to be approximately 9 mm thick.

PDMS-IL samples for swelling and optical studies were prepared in a similar manner, except that CB was removed during the mixing stage. The slurries were transferred to the 30 mm × 7.5 mm × 1 mm mold and then cured at 100 °C for 2 hours.

Samples for tensile tests were prepared in a tensile specimen mold with gauge length of 23 mm, width of 4 mm and thickness of 2 mm. Adequate amount of slurry was placed on one side of the mold and then slowly pushed to fill the mold. When transferring and reshaping the slurries, no hand mixing should be conducted to avoid the bubbles. The sample surface was flattened with a blade. Samples were cured at 100 °C for 2 hours.

Conductivity Measurement

The electrical conductivity of cured bulk samples was measured using the four-probe method with a source meter Keithley 2450 (Tektronix, Inc., USA) at room temperature. Voltage values were recorded as the current varied from -10^{-5} to 10^{-5} A in 200 steps, and a linear fit of the current-voltage curve was used to derive the resistance. The conductivity of the composites was calculated using equation (2.12).

Tensile Test

Young's modulus and elongation at break were measured in a universal tensile testing machine Zwick (ZwickRoell GmbH & Co. KG, Germany). Tensile tests were carried out with a strain rate of 1% per second. For the in situ electrical measurements, a Keithley 2450 was connected to the tensile sample with copper foils held in the tensile clamps during testing. The resistance measurement was carried out at a constant current of 10^{-3} A, and the measured resistance was recorded every second with the KickStart software.

Swelling and Transmittance

Swelling experiments evaluated the cross-linking density of the composites. Samples with an initial weight m_0 were soaked in de-ionized water for 24 hours at room temperature. Water on the sample surface was removed to obtain the swollen weight m_{sw}. After drying at room temperature for 24 hours, the samples had a mass m_{ex}. Equation (2.20) was used to calculate the swelling ratio.

Optical Microscopy

Composite samples were analyzed using a Zeiss AxioScope A.1 microscope (Zeiss, Germany). All images were taken using reflected light in bright field and recorded with an Axiocam 105 color camera at magnifications of 100 to 500x.

Rheological Measurement

The rheological properties of the uncured precursor mixtures were characterized with a TA Instruments Discovery HR-3 Rheometer (TA Instruments, USA). Parallel plates with diameters of 20 mm were used at a fixed gap height of 300 μm. Viscosities were measured in rotational mode at shear rates from 0.1 to 100 s^{-1}. Storage and loss moduli were measured in oscillatory mode within the viscoelastic range at oscillation frequencies from 0.1 to 100 $rad \cdot s^{-1}$. All measurements were done at 25 °C, controlled with a Peltier element.

4.2 Results and Discussion

First, the influence of IL in tuning the electrical and mechanical properties of the composites is discussed. Figure 4.1 illustrates the effect of IL on the electrical conductivities of the composites prepared by mixing the liquid PDMS precursor with CB at a constant volume fraction of 9% and an increasing amount of IL (indicated as the mass ratio between the IL and CB contents).

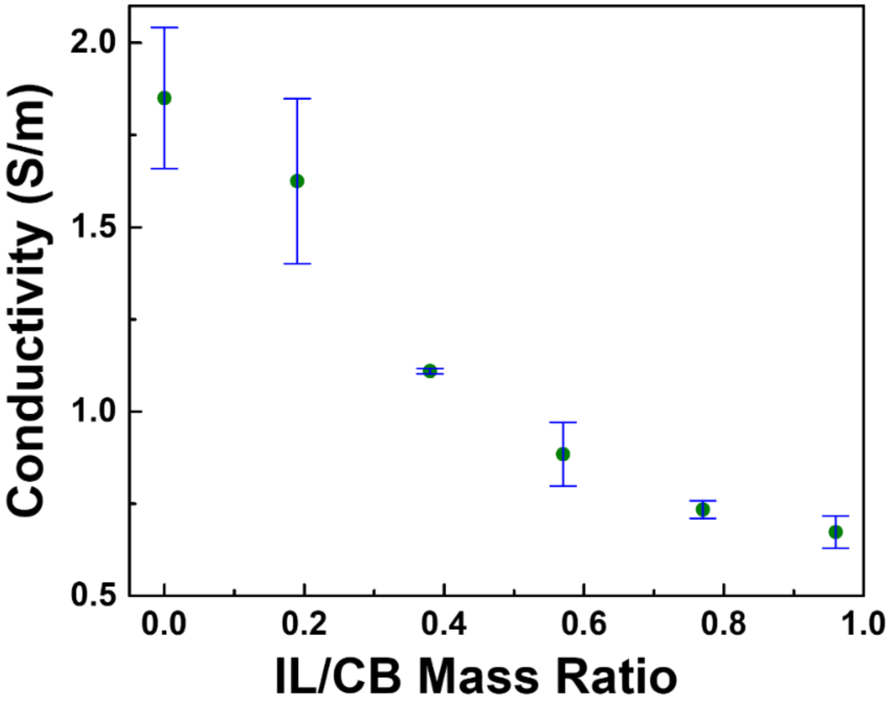

Figure 4.1. Electrical conductivities of PDMS-CB composites with 9 vol-% CB and varying IL [EMIM][TFSI] loadings at room temperature.

Conductivity decreased with increasing IL content, but the difference between PDMS-CB and PDMS-CB-IL-5 is within one order of magnitude. This result is contrary to the observation reported by Hassouneh et al. that IL [EMIM][TFSI] increased the dispersion of CNTs and led to an increase in electrical conductivity.[102] This result also differs from the conclusion reported by Narongthong et al. that the IL DMIC has a positive effect on increasing the conductivity of SBR-CB composites.[103] In this study, the IL reduced the electrical conductivity of the composite, probably because when the CB filler loading is high, the IL does not significantly improve the dispersion of CB fillers, but modifies the conductive CB network structure or the contact resistances between the CB particles, or both.

The stress-strain curves of the elastomer composites and pure PDMS elastomer are shown in Figure 4.2(a), and the values of Young's modulus and elongation at break are shown in Figure 4.2(b).

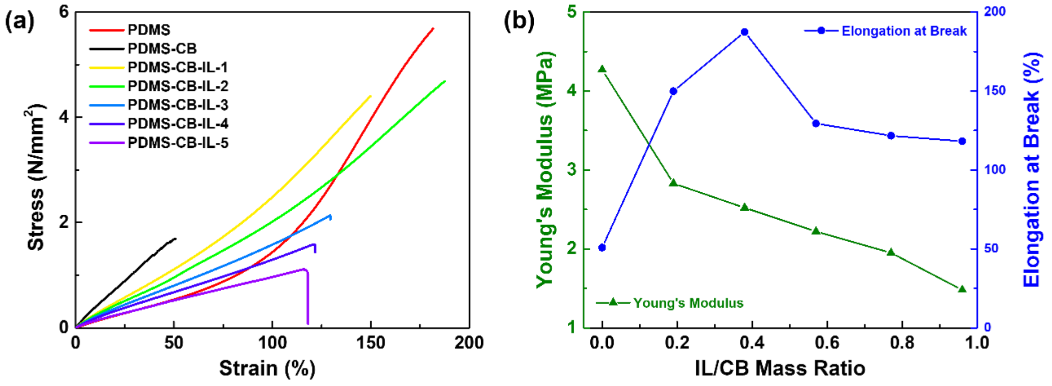

Figure 4.2. (a) Stress-strain curves of PDMS-CB-IL composites with different IL contents. (b) Influence of IL on the Young's modulus and maximum elongation of as-prepared PDMS-CB-IL composites.

Pure PDMS shows a classic elastomer stress-strain curve colored in red. The addition of CB fillers alone makes the composite "brittle", increasing the Young's modulus but decreasing the elongation at break of the composites.[182] As a result, the Young's modulus of PDMS increased from 1.22 MPa to 4.27 MPa with the addition of CB, and the elongation at break of PDMS decreased from 180 % to 50 %. By adding different amounts of IL to the PDMS-CB mixtures, a clear trend of decrease in Young's modulus of the PDMS-CB composites can be observed, from 4.27 MPa for the PDMS-CB composite to 1.48 MPa for the PDMS-CB-IL-5 composite. The addition of IL initially increased the elongation at break of the PDMS-CB composites, and the maximum value of about 180% was observed for the PDMS-CB-IL-2 composite, which is comparable to that of the pure PDMS elastomer. Further increase in the concentration of IL leads to a decrease in the elongation at break. This result means that the addition of a suitable amount of IL can compensate the stiffness caused by the introduction of CB fillers and adapt the PDMS-CB composites to larger deformation.

Figure 4.1 and 4.2 show that the addition of IL changes the electrical and mechanical properties of PDMS-CB composites, which could be the result of IL modified composite structures. To further understand the role of IL in tuning the composite structures, it is important to know how the electrical properties change as a function of strain. For this purpose, the change in resistance as a function of strain was measured. Figure 4.3 shows the evolution of resistance versus tensile strain for the PDMS-CB and PDMS-CB-IL composites. The samples were loaded at a strain rate of 1 % per second, and for each cycle, the maximum strain increase is 10%, as shown in Figure 4.3(a). The experiments were terminated when either the tensile sample broke or was loaded for 10 cycles. Figure 4.3(b)-(d) shows the changes in resistance normalized to the resistance at zero strain. The initial resistance R_0 was used as the reference for calculating the resistance change for all cycles.

Composites without IL failed at strains above 50%. The resistance of PDMS-CB composites increased reversibly at strains below 40%, but an irreversible fraction of $\Delta R_p/R_0 \approx 0.1$ remained after straining to 50%. The changes in resistance of the PDMS-CB-IL-2 composite were similar to those of the PDMS-CB composite for strains below 50%. The PDMS-CB-IL-4 composite showed the largest irreversible fraction, approximately 40% after 50% strain. The reversible changes in resistance at strains below 40% for the composites with and without IL are due to macroscopic changes in sample geometry without structural damage. As the strain increased beyond 50 %, the irreversible change in electrical properties of IL-containing composites became more pronounced. The PDMS-CB-IL-2 and PDMS-CB-IL-4 composites retained an irreversible resistance change after straining beyond 50 %, reaching $\Delta R_{\mathrm{p}}/R_0 \approx 1$ and 2 after 100 % strain, respectively. Similar irreversible changes ($\Delta R_{\mathrm{p}}/R_0 \approx 2$) have been reported previously for PEDOT:PSS/iTPU samples at 50 % strain.[183] The PDMS-CB-IL-4 composite showed a reduced resistance change at 100% strain compared to the PDMS-CB-IL-2 composite, indicating that the excess IL may also reduce the electrical sensitivity of the composite to strain, which may have a negative impact on the use of the as-prepared composite as a sensor. It is likely that the overall change in resistance above 50 % strain is due to a combination of reversible deformation and permanent microstructural damage, where the IL weakens the composite structure and the stress further destroys the structure.

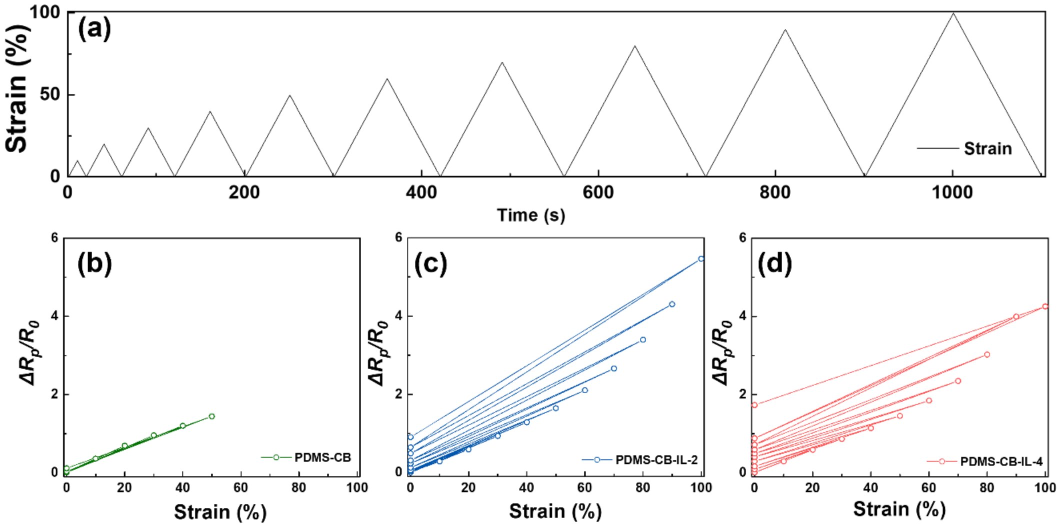

Figure 4.3. (a) The strain pattern of the cyclic strain tests with 10 % strain increase per cycle to 100% strain of the specimens. (b-d) Relative resistance changes versus strain of PDMS-CB, PDMS-CB-IL-2 and PDMS-CB-IL-4 composites. The incremental strain was 10 % for each cycle, and the resistance was recorded at maximum strain.

The strong effects of small amounts of IL on both mechanical and electrical properties suggest that IL modifies the structure of PDMS-CB composites. In the following, swelling and rheological experiments are used to discuss the effects of

IL on the PDMS matrix and CB conductive networks. To understand the interaction between PDMS and IL, a swelling experiment was performed to analyze the cross-linking density of PDMS as a function of IL content. De-ionized water was used as the swelling solvent, and the swelling ratios of PDMS and PDMS with different amounts of IL solid samples in de-ionized water are shown in Figure 4.4(a).

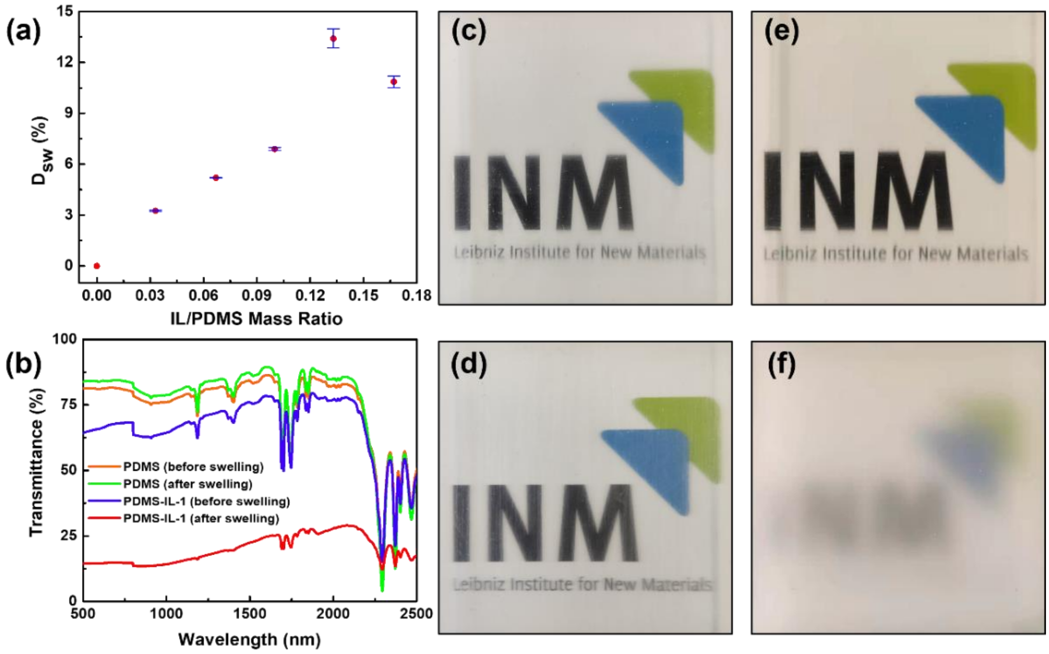

Figure 4.4. (a) Swelling of pure PDMS and PDMS-IL samples in the de-ionized water at room temperature. (b) Optical transmittance of pure PDMS and PDMS-IL-1 before and after swelling. (c) and (d) Optical comparison of pure PDMS before and after swelling, respectively. (e) and (f) Optical comparison of PDMS-IL-1 before and after swelling, respectively.

The swelling of pure PDMS was negligible, and there was no visible change in optical transparency, as shown in Figure 4.4(c) and (d). Figure 4.4(b) shows that the PDMS-IL samples had lower transmittance than the pure PDMS sample before swelling. The presence of IL changes the swelling property of PDMS in de-ionized water, and the swelling ratio of PDMS increased from 0 to 13 % with increasing IL content, corresponding to PDMS-IL and PDMS-IL-4, respectively. For PDMS-IL-5, the swelling ratio decreased to 10 %. Swelling increased optical scattering in the PDMS-IL systems. The optical effect was reversible, allowing switching between semi-transparent (Figure 4.4(e)) and opaque (Figure 4.4(f)) states by swelling and drying, and the comparison of transmission curves colored in red and blue is shown in Figure 4.4(b). The swelling experimental result is consistent with the results of Sinawang et al. who suggested that IL reduces the cross-linking density and thus increases the swelling ratio.[184]

To further investigate the transparency of PDMS-IL samples altered by swelling, light microscopy was used to characterize the surface morphology of PDMS and PDMS-IL-1 samples under dry and swelling conditions. As shown in Figure 4.5(a) and (b), the pure PDMS samples showed no obvious change after swelling or drying. In contrast, the inset image in Figure 4.5(c) shows that the addition of IL resulted in the formation of "pores" directly on the surface. A possible explanation is that the molecular solubility of the IL in the PDMS is limited and some of it formed a separate phase distributed in small droplets. The pores appeared larger after swelling, as shown in Figure 4.5(d). Tiwari et al. also reported that the addition of much larger amounts of IL (10 vol-%) leads to the formation of microscopic IL droplets of about 1 μm in diameter, and the spherical IL inclusions can be clearly observed within the polymer matrix by SEM.[185] This phase separation between the PDMS and IL changes the overall swelling behavior of the material. It is likely that the "pores" in Figure 4.5(c) swell strongly in the presence of water. This explains the change in turbidity caused by swelling, as water droplets create local refractive index contrasts. The sample weights after drying m_{ex} were within 99.2 % of the initial weights m_0 for all PDMS-IL samples tested in Figure 4.4(a). There is no significant change in the weight of the IL-containing material before swelling and after drying, suggesting that the IL may remain in the bulk with limited leaching, while only water is largely removed during drying.

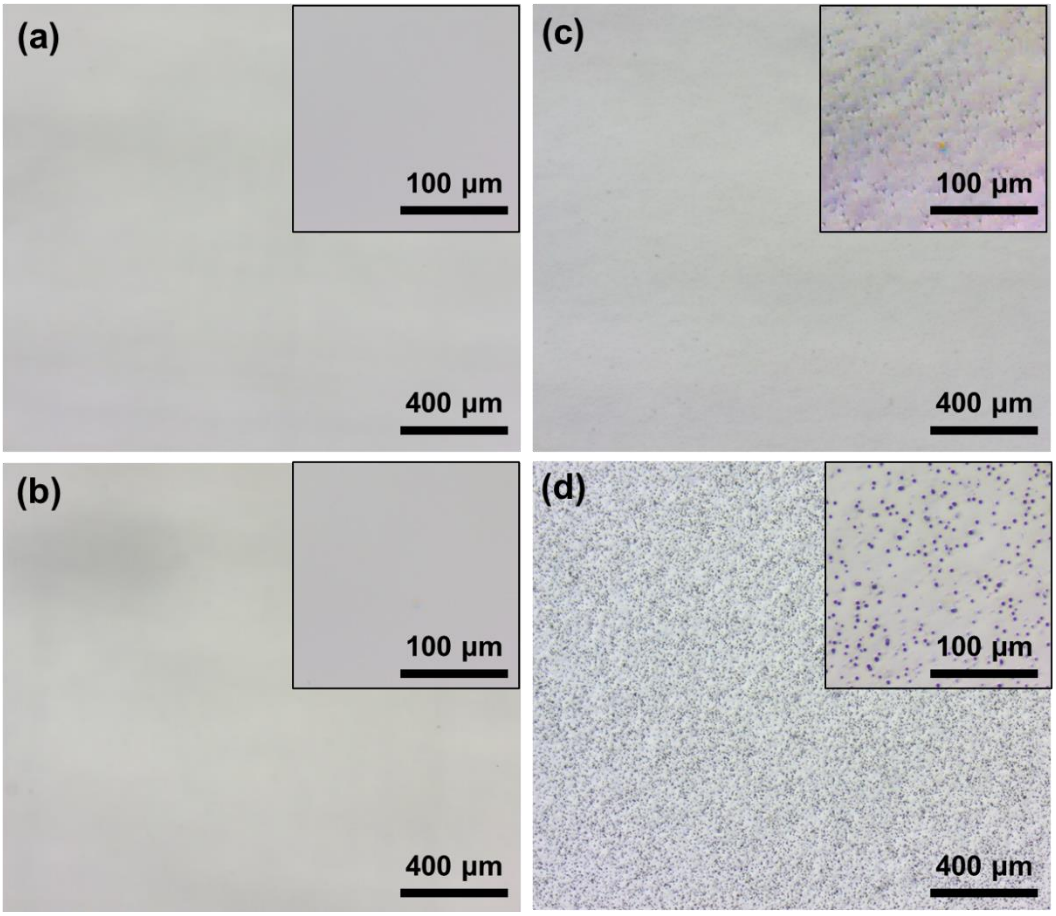

Figure 4.5. Microstructural effects of water on PDMS and PDMS-IL-1 samples. Optical micrographs of pure PDMS (a) in the dry and (b) in the swollen state show no visible changes. Optical micrographs of PDMS-IL-1 in (c) the dry and (d) the swollen state indicate the formation of local structure due to IL addition and grew into larger droplets upon swelling.

The previous results suggest that in the PDMS-IL system, the addition of IL reduces the cross-linking density of the polymer matrix, and the formation of phase-separated droplets changes the structure of the polymer matrix. The electrical and mechanical properties of PDMS-CB-IL composites are strongly influenced by the internal structure formed by the CB and IL in the polymer matrix. However, the interaction between the IL and the CB remained unclear. The rheological properties of the PDMS-IL and PDMS-CB-IL precursor mixtures were investigated to understand how the IL affects the interactions between PDMS and CB. It is assumed that the curing process of the samples only freezes the structure of the viscoelastic precursor, but does not alter the networks formed by CB and IL.

As shown in Figure 4.6(a), the pure PDMS has the lowest viscosity, and the viscosity increases with the addition of IL to the PDMS-IL system. Marwanta *et al.* suggested that IL strongly interacts with the PDMS chains and thus increasing the viscosity.[186] Based on the light microscopy results, the IL partially forms dispersed droplets and can be considered as a soft filler, thus increases the viscosity due to higher network strength, as claimed by Ankit *et al.*[185] In contrast, the addition of IL decreases the viscosity of the PDMS-CB composite, as shown in Figure 4.6(b).Unlike as a soft filler in the pure PDMS matrix, the role of IL changes with the presence of CB in the PDMS-CB system.

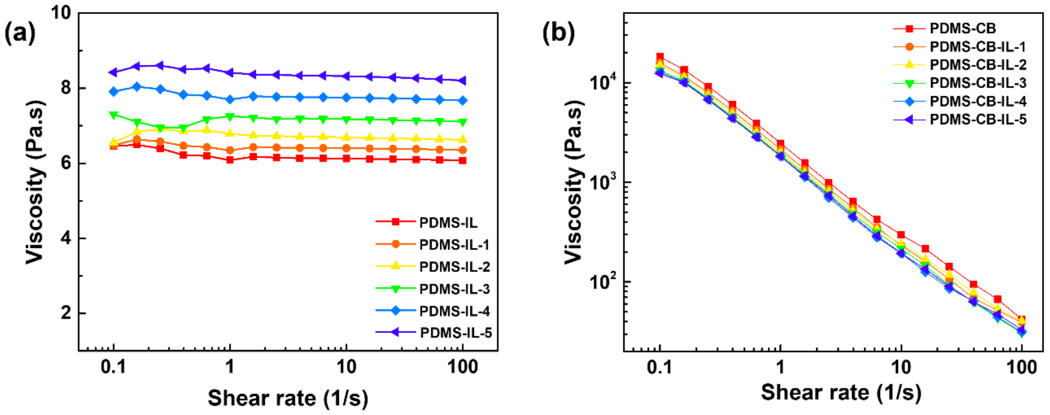

Figure 4.6. Shear viscosities dependence on the applied shear rate of (a) PMDS-IL precursor mixtures and (b) PDMS-CB-IL precursor mixtures.

The storage and loss moduli of PDMS-IL samples are strongly frequency dependent. PDMS with different amounts of IL show similar storage and loss moduli values that are difficult to distinguish, as shown in Figure 4.7(a) and (b). In contrast, the reduction in storage and loss moduli among different PDMS-CB-IL composites was evident. As shown in Figure 4.7(c) and (d), for the PDMS-CB-IL system, the storage and loss moduli decreased significantly with increasing IL, indicating a weaker internal structure due to the introduction of IL into the

PDMS-CB system. And even with the smallest amount of IL addition, the decrease in storage and loss moduli is significant.

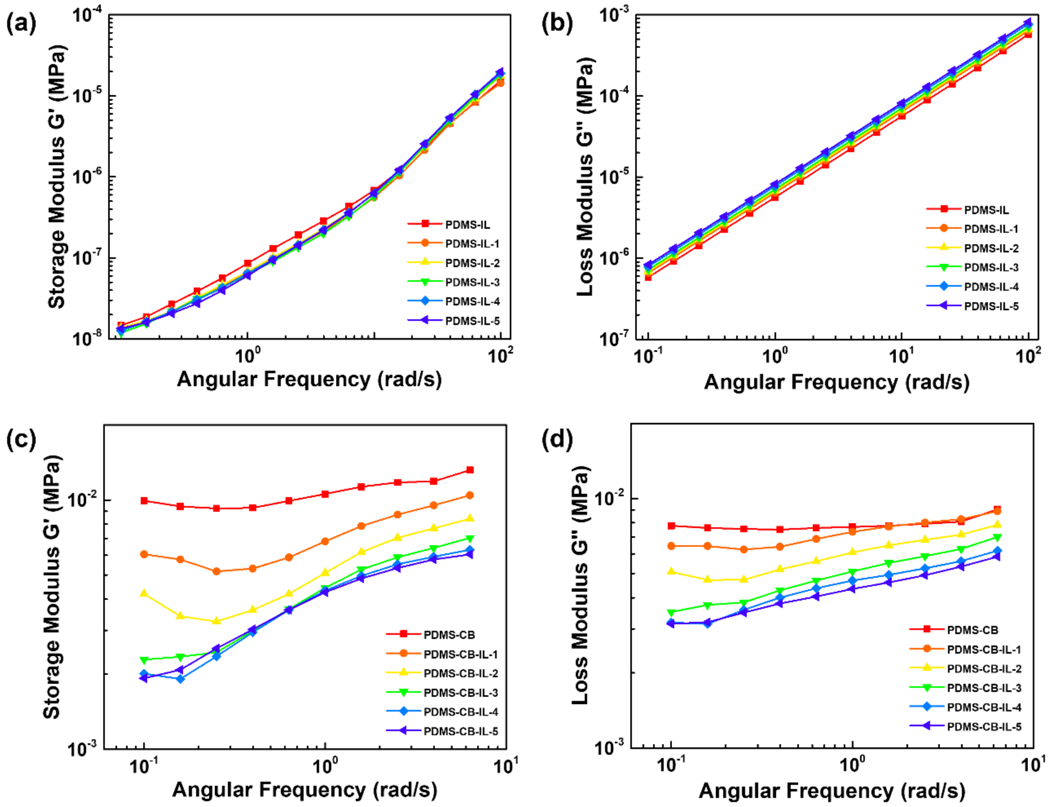

Figure 4.7. Frequency dependent (a) storage and (b) loss moduli of the PDMS-IL composites. Frequency dependent (c) storage and (d) loss moduli of the PDMS-CB-IL composites.

The decrease in moduli can be explained by the affinity of IL for the non-polar CB fillers, as suggested by Laskowska et al.[187] The fraction of IL that is not soluble in PDMS is likely to be adsorbed on the CB surface, thus altering the agglomeration behavior of CB and the solid-liquid hydrodynamics in the mixture. The IL adsorbed at the CB-CB interfaces increases the electrical contact resistance between the filler particles, weakens the filler network and the mechanical strength of the agglomerates, and IL between CB and PDMS may also reduce the hydrodynamic CB-PDMS coupling, as demonstrated in Figure 4.8. The observation in this chapter is consistent with the weakened filler-rubber coupling previously reported by Zhang et al. for other imidazolium-based ILs.[188]

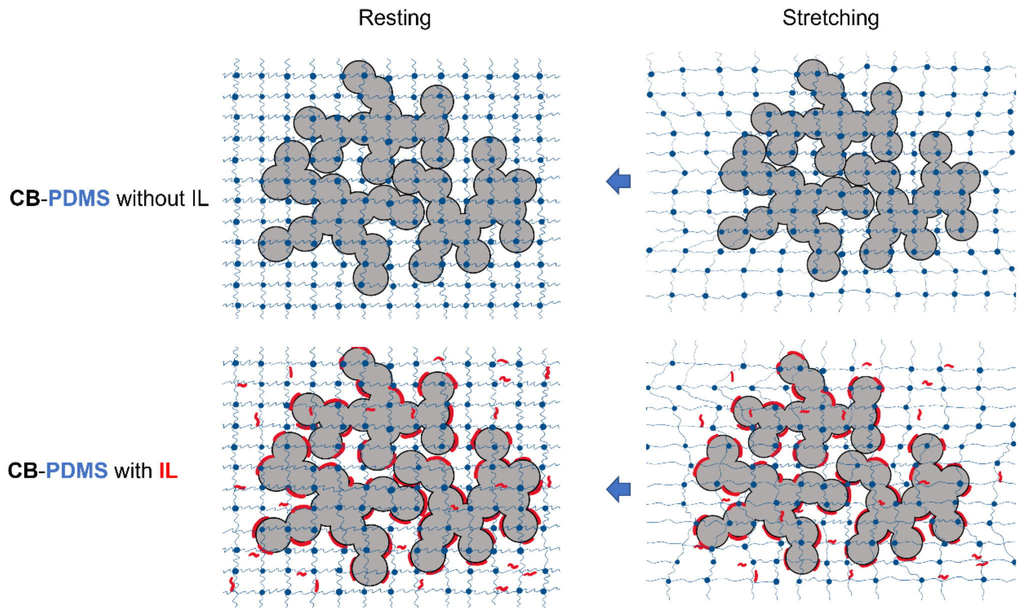

Figure 4.8. Schematic representation of the suggested microstructure of the PDMS-CB composite with and without ionic liquid (IL) at zero ("resting") and finite ("stretching") strain. PDMS chains interact with the CB surface and increase the elastic modulus. The IL molecules (a) reduce the cross-linking degree of the PDMS and (b) adsorb on the CB surfaces, increasing the electrical contact resistance between the particles, and facilitating a relative PDMS-CB displacement during stretching.

The rheological results are in good agreement with the results for the solid composites, where increasing IL content reduced mechanical strength but increased elongation at break. The stress distribution in PDMS-CB composites with weakened connections between the matrix and filler reduces the overall brittleness, and the CB fillers with contacts "lubricated" by the IL are more likely to rearrange when strained (and when the stress is released) than to permanently fracture.

4.3 Summary

This chapter focused on tuning the structures of PDMS-CB composites by the addition of IL [EMIM][TFSI]. Conductive PDMS composites with low Young's moduli were prepared using the small amount of IL. The addition of IL decreased the conductivity but increased the stretchability of the PDMS-CB composites. To understand the changes in conductivity and stretchability, the interactions between IL, PDMS and CB were investigated by a combination of rheological and swelling experiments, and optical studies.

The swelling experiments and optical images showed that the IL reduced the cross-linking density and formed phase-separated droplets in the PDMS matrix. And the rheological results of PDMS-IL composites showed that the phase-separated IL droplets acted as soft fillers to increase the viscosity of PDMS. However, the role of IL in the composites was different in the presence of CB. The addition of IL weakened the PDMS-CB structure in terms of lower viscosity and storage modulus, probably because the IL, which is not soluble in PDMS, is probably absorbed at the CB interface, thus increasing the contact resistance of the filler particles and reducing the conductivity. Another possible mechanism is that the addition of IL altered the agglomeration behavior of the CB and reduced the percolation paths, resulting in a decrease in bulk conductivity. More detailed investigations using techniques such as electron microscopy and scattering should be carried out to understand the observations from the rheological results and to verify the above mechanisms.

The relative changes in resistance to strain were not much affected by the IL, and the changes in mechanical properties allow the composites to be used as sensors or electrodes for larger deformations.

5 Conclusion and Outlook

This dissertation focused on tuning the structure and conductivity of PDMS composites in terms of conductive CB fillers and IL [EMIM][TFSI]. The results of this dissertation provided a better understanding in the preparation of elastomer composites with desired properties. Overall, a larger CB aggregate is advantageous to use less fractal filler to reach the percolation threshold. And the stiffness of the PDMS composites caused by the CB fillers can be compensated by a suitable amount of IL.

Chapter 3 studied the influence of CB aggregate size on tuning the conductivity of the PDMS-CB composites. The aggregate size of CB was found to have a significant influence in percolation behavior. More CB fillers with smaller sizes will be used to reach the percolation threshold compared to the larger ones. And for composites with the same concentration of unground CB and ball-milled CB, composites with unground CB showed a higher conductivity. The possible explanation is that ball-milling increased the proportion of smaller aggregates, which tended to agglomerate into larger clusters, resulting in fewer conductive paths, thus changing the conductive network structure. The agglomeration behavior difference of unground and ball-milled CB in the PDMS matrix caused by the CB aggregate size distributions is also confirmed by the scattering measurements.

The hierarchical structure of CB is formed partially by pre-formed structures (aggregates) and partially by structures formed during composite formation (agglomeration). The size of the CB aggregate is important because it not only determines the agglomeration behavior of CB in the polymer matrix, but also further changes the percolation behavior of CB geometrically. A larger CB aggregate will result in less material being used to reach the percolation threshold and higher conductivity.

Chapter 4 focused on role of IL in tuning the structures and properties of PDMS-CB composites. Conductive PDMS-CB composite with low Young's modulus and good stretchability were prepared using the small amount of IL. The small amount of IL addition does not significantly change the resistance response behavior, although the IL reduces the overall conductivity of the composites compared to PDMS-CB composites without IL.

The IL tuned the structure of the PDMS-CB composites in several aspects. The swelling experiments confirmed that the IL reduced the cross-linking density of PDMS, and optical images showed that the IL also formed phase-separated droplets in the PDMS matrix. The phase-separated IL droplets acted as soft fillers to increase the viscosity of PDMS in the PDSM-IL composite. However, the role of IL in the PDMS-CB composites was different in the presence of CB. The addition of IL weakened the PDMS-CB structure in terms of a lower viscosity, storage and loss moduli, probably because the portion of IL, which is not soluble in PDMS, is probably absorbed at the CB interface, increasing the contact resistance between the CB fillers, thus reducing the conductivity. Meanwhile, the addition of IL may alter the agglomeration behavior of the CB and reduce the percolation paths, thereby reducing the conductivity. Both mechanisms reduce the bulk conductivity but may also reduce the change in resistance with strain by making the network less brittle.

Conductive elastomer composites are a large and complex topic. This dissertation is only a small attempt, many works regarding the structures and properties should be explored and solved. Based on the results of this dissertation, future work may include, but is not limited to:

As an extension of Chapter 3,

1. Scattering techniques should be further applied to understand the correlations between structural and electrical properties. The fractal dimension

of agglomerates decreased with increasing filler volume fraction. Overall, there is a difference in the fractal dimension when comparing the composites with the same amount of unground CB and the ball-milled CB. The scattering experiments should be repeated and statistically evaluated to confirm this observation.

2. In order to study the change of the conductive network under strain, in-situ scattering measurements coupled with tensile test should be performed on the composite samples. As reported by Shinohara et al., the 2D scattering pattern will change as a reflection during deformation.[189] The change in fractal dimension with stress should be measured and interpreted together with the change in 2D scattering pattern to see if the fractal dimension can be an indicator of sample deformation. This would be beneficial to further reveal the formation of conductive networks and explain how the conductive networks change under deformation.

As an extension of Chapter 4,

1.In addition to the optically visible phase separation observed in Chapter 4, techniques such as electron microscopy and scattering should be used to understand whether phase separation also occurs in the material below the level of optical visibility, or how the ionic liquid is otherwise distributed in the material.

2. The results of Chapter 4 showed that the interfaces between the different phases are also important in the elastomer composites, because the interface properties can determine the agglomeration behavior of the fillers, thereby changing the mechanical and electrical properties of the composites. In order to obtain composites with desired properties, modification of the filler-polymer interface will be an effective way. It will be interesting to study how the hydrophobicity/hydrophilicity of the IL modifies the interfaces of the fillers and further affects the filler agglomeration in the polymer matrix.

Reference

1. Wang, Y.; Ameer, G. A.; Sheppard, B. J.; Langer, R., A Tough Biodegradable Elastomer. *Nat. Biotechnol.* **2002,** *20* (6), 602-606.

2. Carlson, J. D.; Jolly, M. R., MR Fluid, Foam and Elastomer Devices. *Mechatronics* **2000,** *10* (4-5), 555-569.

3. Bhowmick, A. K.; Bhattacharya, M.; Maiti, M., Elastomer Nanocomposites. *Rubber Chem. Technol.* **2008,** *81* (3), 384-469.

4. Mathew, M.; Schilling, T.; Oettel, M., Connectivity Percolation in Suspensions of Hard Platelets. *Phys. Rev. E* **2012,** *85* (6 Pt 1), 061407.

5. Yuan, J.; Luna, A.; Neri, W.; Zakri, C.; Schilling, T.; Colin, A.; Poulin, P., Graphene Liquid Crystal Retarded Percolation for New High-k Materials. *Nat. Commun.* **2015,** *6*, 8700.

6. Shang, S.; Yue, Y.; Wang, X., Piezoresistive Strain Sensing of Carbon Black /Silicone Composites Above Percolation Threshold. *Rev. Sci. Instrum.* **2016,** *87* (12), 123910.

7. Dang, Z.-M.; Yuan, J.-K.; Zha, J.-W.; Zhou, T.; Li, S.-T.; Hu, G.-H., Fundamentals, Processes and Applications of High-Permittivity Polymer–Matrix Composites. *Prog. Mater. Sci.* **2012,** *57* (4), 660-723.

8. Sandler, J. K. W.; Kirk, J. E.; Kinloch, I. A.; Shaffer, M. S. P.; Windle, A. H., Ultra-low Electrical Percolation Threshold in Carbon-nanotube-epoxy Composites. *Polymer* **2003,** *44* (19), 5893-5899.

9. Luo, Y.; Xiong, S. Y.; Zhang, F.; He, X. X.; Lu, X.; Peng, R. T., Preparation of Conductive Polylactic Acid/High Density Polyethylene/Carbon Black Composites with Low Percolation Threshold by Locating the Carbon Black at the Interface of Co‐continuous Blends. *J. Appl. Polym. Sci.* **2020,** *138* (17), 50291.

10. Cattin, C.; Hubert, P., Piezoresistance in Polymer Nanocomposites with High Aspect Ratio Particles. *ACS Appl. Mater. Interfaces* **2014,** *6* (3), 1804-1811.

11. Shi, G.; Zhao, Z.; Pai, J. H.; Lee, I.; Zhang, L.; Stevenson, C.; Ishara, K.; Zhang, R.; Zhu, H.; Ma, J., Highly Sensitive, Wearable, Durable Strain Sensors and Stretchable Conductors Using Graphene/Silicon Rubber Composites. *Adv. Funct. Mater.* **2016,** *26* (42), 7614-7625.

12. Xu, Z.; Bykova, J.; Baniasadi, M.; Moreno, S.; Zhou, Z.; Das, N.; Bandi, S.; Xi, Y.; Qian, D.; Baughman, R. H.; Minary-Jolandan, M., Bioinspired Multifunctional Ceramic Platelet-Reinforced Piezoelectric Polymer Composite *Adv. Eng. Mater.* **2017,** *19* (2), 1600570.

13. Boland, C. S.; Khan, U.; Ryan, G.; Barwich, S.; Charifou, R.; Harvey, A.; Backes, C.; Li, Z.; Ferreira, M. S.; Mobius, M. E.; Young, R. J.; Coleman, J. N., Sensitive Electromechanical Sensors Using Viscoelastic Graphene-polymer Nanocomposites. *Science* **2016,** *354* (6317), 1257-1260.

14. Meyer, H.; van der Schoot, P.; Schilling, T., Percolation in Suspensions of Polydisperse Hard Rods: Quasi Universality and Finite-size Effects. *J. Chem. Phys.* **2015,** *143* (4), 044901.

15. Punetha, V. D.; Rana, S.; Yoo, H. J.; Chaurasia, A.; McLeskey, J. T.; Ramasamy, M. S.; Sahoo, N. G.; Cho, J. W., Functionalization of Carbon Nanomaterials for Advanced Polymer Nanocomposites: A Comparison Study Between CNT and Graphene. *Prog. Polym. Sci.* **2017,** *67*, 1-47.

16. Potts, J. R.; Dreyer, D. R.; Bielawski, C. W.; Ruoff, R. S., Graphene-based polymer nanocomposites. *Polymer* **2011,** *52* (1), 5-25.

17. Schilling, T.; Jungblut, S.; Miller, M. A., Depletion-induced percolation in networks of nanorods. *Phys. Rev. Lett.* **2007,** *98* (10), 108303.

18. Otten, R. H.; van der Schoot, P., Continuum Percolation of Polydisperse Nanofillers. *Phys. Rev. Lett.* **2009,** *103* (22), 225704.

19. Chatterjee, A. P., Connectedness percolation in monodisperse rod systems: clustering effects. *J. Phys.: Condens. Matter* **2011,** *23* (37), 375101.

20. Otten, R. H.; van der Schoot, P., Connectivity Percolation of Polydisperse Anisotropic Nanofillers. *J. Chem. Phys.* **2011,** *134* (9), 094902.

21. Jadrich, R.; Schweizer, K. S., Percolation, Phase Separation, and Gelation in Fluids and Mixtures of Spheres and Rods. *J. Chem. Phys.* **2011,** *135* (23), 234902.

22. Otten, R. H.; van der Schoot, P., Connectedness Percolation of Elongated Hard Particles in an External Field. *Phys. Rev. Lett.* **2012,** *108* (8), 088301.

23. Nigro, B.; Grimaldi, C.; Miller, M. A.; Ryser, P.; Schilling, T., Tunneling Conductivity in Composites of Attractive Colloids. *J. Chem. Phys.* **2012,** *136* (16), 164903.

24. Mutiso, R. M.; Sherrott, M. C.; Li, J.; Winey, K. I., Simulations and Generalized Model of the Effect of Filler Size Dispersity on Electrical Percolation in Rod Networks. *Phys. Rev. B* **2012,** *86* (21), 214306.

25. Nigro, B.; Grimaldi, C.; Ryser, P.; Chatterjee, A. P.; van der Schoot, P., Quasiuniversal Connectedness Percolation of Polydisperse Rod Systems. *Phys. Rev. Lett.* **2013,** *110* (1), 015701.

26. Nigro, B.; Grimaldi, C.; Miller, M. A.; Ryser, P.; Schilling, T., Depletion-interaction Effects on the Tunneling Conductivity of Nanorod Suspensions. *Phys. Rev. E* **2013,** *88* (4), 042140.

27. Chatterjee, A. P.; Grimaldi, C., Random Geometric Graph Description of Connectedness Percolation in Rod Systems. *Phys. Rev. E* **2015,** *92* (3), 032121.

28. Dixit, M.; Meyer, H.; Schilling, T., Connectivity Percolation in Suspensions of Attractive Square-well Spherocylinders. *Phys. Rev. E* **2016,** *93* (1), 012116.

29. Lahaye, J.; Prado, G., Morphology and Internal Structure of Soot and Carbon Blacks. In *Particulate Carbon: Formation During Combustion*, Siegla, D. C.; Smith, G. W., Eds. Springer US: Boston, MA, 1981; pp 33-55.

30. Drogin, I., Carbon Black. *J. Air Pollut. Control Assoc.* **1968,** *18* (4), 216-228.

31. COAKER, A. W. M., *Processing and Finishing of Polymeric Materials*. 2012; p 254.

32. Donnet, J.-B., *Carbon Black: Science and Technology*. CRC Press: 1993.

33. Warren, B. E., X‐Ray Diffraction Study of Carbon Black. *J. Chem. Phys.* **1934,** *2* (9), 551-555.

34. Evtugyn, G.; Hianik, T., Chapter 9 - Electroanalytical Bioplatforms Based on Carbon Nanostructures as New Tools for Diagnosis. In *Nanotechnol. Biosens.*, Nikolelis, D. P.; Nikoleli, G.-P., Eds. Elsevier: 2018; pp 269-306.

35. Koga, T.; Takenaka, M.; Aizawa, K.; Nakamura, M.; Hashimoto, T., Structure Factors of Dispersible Units of Carbon Black Filler in Rubbers. *Langmuir* **2005,** *21* (24), 11409-11413.

36. Miyauchi, S. N.; Sorimachi, Y.; Mitsui, M.; Akihide, H.; Ohkita, K., Electrical Properties of Carbon-black Grafted with Polymers Using an Anionic Catalyst. *J. Appl. Polym. Sci.* **1984,** *29* (1), 251-259.

37. Kraus, G.; Jansen, J., New Methods for Estimating Dispersibility of Carbon Blacks in Rubber. *Rubber Chem. Technol.* **1980,** *53* (1), 48-65.

38. Lu, S.; Chung, D. D. L., Viscoelastic Behavior of Carbon Black and Its Relationship with the Aggregate Size. *Carbon* **2013,** *60*, 346-355.

39. Herd, C. R.; Gruber, T. C., Anisometry Measurements in Carbon Black Aggregate Populations. *Rubber Chem. Technol.* **1997,** *70* (5), 727-746.

40. Naderi, M., Chapter Fourteen - Surface Area: Brunauer–Emmett–Teller (BET). In *Progress in Filtration and Separation*, Tarleton, S., Ed. Academic Press: Oxford, 2015; pp 585-608.

41. Lowell, S.; Shields, J. E., Langmuir and BET Theories (Kinetic Isotherms). In *Powder Surface Area and Porosity*, Lowell, S.; Shields, J. E., Eds. Springer Netherlands: Dordrecht, 1991; pp 14-29.

42. Christopher, G.; Anbu Kulandainathan, M.; Harichandran, G., Comparative Study of Effect of Corrosion on Mild Steel with Waterborne Polyurethane Dispersion Containing Graphene Oxide Versus Carbon Black Nanocomposites. *Prog. Org. Coat.* **2015,** *89*, 199-211.

43. López-de-Uralde, J.; Ruiz, I.; Santos, I.; Zubillaga, A.; Bringas, P. G.; Okariz, A.; Guraya, T. In *Automatic Morphological Categorisation of Carbon Black Nano-aggregates*, Database and Expert Systems Applications, Berlin, Heidelberg, 2010//; Bringas, P. G.; Hameurlain, A.; Quirchmayr, G., Eds. Springer Berlin Heidelberg: Berlin, Heidelberg, 2010; pp 185-193.

44. Mandelbrot, B. B., *Fractals: Form, Chance, and Dimension*. W.H.Freeman & Company: 1977.

45. Witten, T. A.; Sander, L. M., Diffusion-Limited Aggregation. *Phys. Rev. B* **1983,** *27* (9), 5686-5697.

46. Thompson, D. W.; Thompson, D. A. W., *On Growth and Form*. Cambridge university press Cambridge: 1942; Vol. 2.

47. Witten, T. A.; Sander, L. M., Diffusion-Limited Aggregation, a Kinetic Critical Phenomenon. *Phys. Rev. Lett.* **1981,** *47* (19), 1400-1403.

48. Forrest, S. R.; Witten, T. A., Long-range Correlations in Smoke-particle Aggregates. *J. Phys. A: Math. Gen.* **1979,** *12* (5), L109-L117.

49. Mansfield, M. L.; Douglas, J. F., Numerical Path-integration Calculation of Transport Properties of Star Polymers and Theta-DLA Aggregates. *Condens. Matter Phys.* **2002,** *5*, 249.

50. Meakin, P., Diffusion-controlled Cluster Formation in 2—6 Dimensional Space. *Phys. Rev. A* **1983,** *27* (3), 1495-1507.

51. Klüppel, M., The Role of Disorder in Filler Reinforcement of Elastomers on Various Length Scales. In *Filler-Reinforced Elastomers Scanning Force Microscopy*, Capella, B.; Geuss, M.; Klüppel, M.; Munz, M.; Schulz, E.; Sturm, H., Eds. Springer Berlin Heidelberg: Berlin, Heidelberg, 2003; pp 1-86.

52. Kahnert, M.; Kanngießer, F., Modelling Optical Properties of Atmospheric Black Carbon Aerosols. *J. Quant. Spectrosc. Radiat. Transfer* **2020,** *244*, 106849.

53. Deslandes, Y.; Whitmore, M. D.; Bluhm, T. L.; Hokansson, A., Characterization of Carbon Black Filled Polymers Using Small Angle X-Ray Scattering and Transmission Electron Microscopy: A Comparative Study. *J. Dispersion Sci. Technol.* **1988,** *9* (3), 235-257.

54. Sahouli, B.; Blacher, S.; Brouers, F.; Sobry, R.; van den Bossche, G.; Darmstadt, H.; Roy, C., SAXS Characterization of Pyrolytic Carbon Blacks. *MRS Online Proc. Libr.* **2011,** *407*, 39.

55. Growney, D. J.; Mykhaylyk, O. O.; Middlemiss, L.; Fielding, L. A.; Derry, M. J.; Aragrag, N.; Lamb, G. D.; Armes, S. P., Is Carbon Black a Suitable Model Colloidal Substrate for Diesel Soot? *Langmuir* **2015,** *31* (38), 10358-69.

56. Zerda, T.; Xu, W.; Zerda, A.; Zhao, Y.; Von Dreele, R., High Pressure Raman and Neutron Scattering Study on Structure of Carbon Black Particles. *Carbon* **2000,** *38* (3), 355-361.

57. Franceschetti, G.; Riccio, D., CHAPTER 3 - Surface Fractal Models. In *Scattering, Natural Surfaces, and Fractals*, Franceschetti, G.; Riccio, D., Eds. Academic Press: Burlington, 2007; pp 61-113.

58. Keefer, K. D., Structure and Growth of Silica Condensation Polymers. In *Silicon-Based Polymer Science*, American Chemical Society: 1989; Vol. 224, pp 227-240.

59. Anitas, E. M., Small-Angle Scattering from Fractals: Differentiating between Various Types of Structures. *Symmetry* **2020,** *12* (1), 65.

60. López-Ruiz, R., Complexity in Biological and Physical Systems. IntechOpen: 2018.

61. Rieker, T. P.; Misono, S.; Ehrburger-Dolle, F., Small-Angle X-ray Scattering from Carbon Blacks: Crossover between the Fractal and Porod Regimes. *Langmuir* **1999,** *15* (4), 914-917.

62. Rieker, T. P.; Hindermann-Bischoff, M.; Ehrburger-Dolle, F., Small-Angle X-ray Scattering Study of the Morphology of Carbon Black Mass Fractal Aggregates in Polymeric Composites. *Langmuir* **2000,** *16* (13), 5588-5592.

63. Ehrburger-Dolle, F.; Bley, F.; Geissler, E.; Livet, F.; Morfin, I.; Rochas, C., Filler Networks in Elastomers. *Macromol. Symp.* **2003,** *200* (1), 157-168.

64. Linnebach, P.; Simone, F.; Rizzello, G.; Seelecke, S., Development, Manufacturing, and Validation of a Dielectric Elastomer Membrane Actuator–driven Contactor. *J. Intell. Mater. Syst. Struct.* **2018,** *30* (4), 636-648.

65. Rizzello, G.; Hodgins, M.; Naso, D.; York, A.; Seelecke, S., Dynamic Modeling and Experimental Validation of an Annular Dielectric Elastomer Actuator With a Biasing Mass. *J. Vib. Acoust.* **2015,** *137* (1), 011005.

66. Schmidt, M.; Ullrich, J.; Wieczorek, A.; Frenzel, J.; Schütze, A.; Eggeler, G.; Seelecke, S., Thermal Stabilization of NiTiCuV Shape Memory Alloys: Observations During Elastocaloric Training. *Shap. Mem. Superelasticity* **2015,** *1* (2), 132-141.

67. Kunze, J.; Prechtl, J.; Bruch, D.; Fasolt, B.; Nalbach, S.; Motzki, P.; Seelecke, S.; Rizzello, G., Design, Manufacturing, and Characterization of Thin, Core-Free, Rolled Dielectric Elastomer Actuators. *Actuators* **2021,** *10* (4), 69.

68. Baltes, M.; Kunze, J.; Prechtl, J.; Seelecke, S.; Rizzello, G., A Bi-stable Soft Robotic Bendable Module Driven by Dilicone Dielectric Elastomer Actuators: Sesign, Characterization, and Parameter Study. *Smart Mater. Struct.* **2022,** *31* (11), 114002.

69. Prechtl, J.; Kunze, J.; Seelecke, S.; Rizzello, G. In *Soft Robotic Module Actuated by Silicone-Based Rolled Dielectric Elastomer Actuators - Modeling and Simulation*, ACTUATOR; International Conference and Exhibition on New Actuator Systems and Applications 2021, 17-19 Feb. 2021; 2021; pp 1-4.

70. Rizzello, G.; Naso, D.; York, A.; Seelecke, S., Closed Loop Control of Dielectric Elastomer Actuators Based on Self-sensing Displacement Feedback. *Smart Mater. Struct.* **2016,** *25* (3), 035034.

71. Rizzello, G.; Naso, D.; York, A.; Seelecke, S., A Self-Sensing Approach for Dielectric Elastomer Actuators Based on Online Estimation Algorithms. *IEEE ASME Trans. Mechatron.* **2017,** *22* (2), 728-738.

72. Neu, J.; Croce, S.; Willian, T.; Hubertus, J.; Schultes, G.; Seelecke, S.; Rizzello, G., Distributed Electro-Mechanical Coupling Effects in a Dielectric Elastomer Membrane Array. *Exp. Mech.* **2022,** *63* (1), 79-95.

73. Croce, S.; Moretti, G.; Neu, J.; Hubertus, J.; Seelecke, S.; Schultes, G.; Rizzello, G. In *Finite Element Modeling and Simulation of a Soft Array of Dielectric Elastomer Actuators*, ASME 2021 Conference on Smart Materials, Adaptive Structures and Intelligent Systems, 2021.

74. Rizzello, G.; Naso, D.; Turchiano, B.; Seelecke, S., Robust Position Control of Dielectric Elastomer Actuators Based on LMI Optimization. *IEEE T. Contr. Syst. T.* **2016,** *24* (6), 1909-1921.

75. Hau, S.; Bruch, D.; Rizzello, G.; Motzki, P.; Seelecke, S., Silicone Based Dielectric Elastomer Strip Actuators Coupled with Nonlinear Biasing Elements for Large Actuation Strains. *Smart Mater. Struct.* **2018,** *27* (7), 074003.

76. Ling, Y.; An, T.; Yap, L. W.; Zhu, B.; Gong, S.; Cheng, W., Disruptive, Soft, Wearable Sensors. *Adv. Mater.* **2020,** *32* (18), e1904664.

77. Gao, W.; Ota, H.; Kiriya, D.; Takei, K.; Javey, A., Flexible Electronics toward Wearable Sensing. *Acc. Chem. Res.* **2019,** *52* (3), 523-533.

78. Yin, R.; Wang, D.; Zhao, S.; Lou, Z.; Shen, G., Wearable Sensors - Enabled Human–Machine Interaction Systems: From Design to Application. *Adv. Funct. Mater.* **2020,** *31* (11), 2008936.

79. Sang, Z.; Ke, K.; Manas-Zloczower, I., Effect of Carbon Nanotube Morphology on Properties in Thermoplastic Elastomer Composites for Strain Sensors. *Compos. Part A Appl. Sci. Manuf.* **2019,** *121*, 207-212.

80. Zhu, Y.; Chen, X.; Chu, K.; Wang, X.; Hu, Z.; Su, H., Carbon Black/PDMS Based Flexible Capacitive Tactile Sensor for Multi-Directional Force Sensing. *Sensors* **2022,** *22* (2), 628.

81. Nankali, M.; Nouri, N. M.; Navidbakhsh, M.; Malek, N. G.; Amindehghan, M. A.; Shahtoori, A. M.; Karimi, M.; Amjadi, M., Highly Stretchable and Sensitive Strain Sensors Based on Carbon Nanotube–elastomer Nanocomposites: The Effect of Environmental Factors on Strain Sensing Performance. *J. Mater. Chem. C* **2020,** *8* (18), 6185-6195.

82. Lee, J.; Kim, S.; Lee, J.; Yang, D.; Park, B. C.; Ryu, S.; Park, I., A Stretchable Strain Sensor Based on a Metal Nanoparticle Thin Film for Human Motion Detection. *Nanoscale* **2014,** *6* (20), 11932-11939.

83. Feng, P.; Ji, H.; Zhang, L.; Luo, X.; Leng, X.; He, P.; Feng, H.; Zhang, J.; Ma, X.; Zhao, W., Highly Stretchable Patternable Conductive Circuits and Wearable Strain Sensors Based on Polydimethylsiloxane and Silver Nanoparticles. *Nanotechnology* **2019,** *30* (18), 185501.

84. Tsuchitani, S.; Sunahara, T.; Miki, H., Dielectric Elastomer Actuators Using Slide-Ring Material® with Increased Permittivity. *Smart Mater. Struct.* **2015,** *24* (6), 065030.

85. Hu, W.; Zhang, S. N.; Niu, X.; Liu, C.; Pei, Q., An Aluminum Nanoparticle–acrylate Copolymer Nanocomposite as a Dielectric Elastomer with a High Dielectric Constant. *J. Mater. Chem. C* **2014,** *2* (9), 1658-1666.

86. Larmagnac, A.; Eggenberger, S.; Janossy, H.; Voros, J., Stretchable Electronics Based on Ag-PDMS Composites. *Sci. Rep.* **2014,** *4*, 7254.

87. Karuthedath, C. B.; Fikri, U.; Ruf, F.; Schwesinger, N., Characterization of Carbon Black Filled PDMS-Composite Membranes for Sensor Applications. *Key Eng. Mater.* **2017,** *753*, 18-27.

88. Chen, J.; Zheng, J.; Gao, Q.; Zhang, J.; Zhang, J.; Omisore, O. M.; Wang, L.; Li, H., Polydimethylsiloxane (PDMS)-Based Flexible Resistive Strain Sensors for Wearable Applications. *Appl. Sci.* **2018,** *8* (3), 345.

89. Qi, D.; Zhang, K.; Tian, G.; Jiang, B.; Huang, Y., Stretchable Electronics Based on PDMS Substrates. *Adv. Mater.* **2021,** *33* (6), e2003155.

90. Gilshteyn, E. P.; Romanov, S. A.; Kopylova, D. S.; Savostyanov, G. V.; Anisimov, A. S.; Glukhova, O. E.; Nasibulin, A. G., Mechanically Tunable Single-Walled Carbon Nanotube Films as a Universal Material for Transparent and Stretchable Electronics. *ACS Appl. Mater. Interfaces* **2019,** *11* (30), 27327-27334.

91. Morent, R.; De Geyter, N.; Axisa, F.; De Smet, N.; Gengembre, L.; De Leersnyder, E.; Leys, C.; Vanfleteren, J.; Rymarczyk-Machal, M.; Schacht, E.; Payen, E., Adhesion Enhancement by a Dielectric Barrier Discharge of PDMS Used for Flexible and Stretchable Electronics. *J. Phys. D: Appl. Phys.* **2007,** *40* (23), 7392-7401.

92. Wang, S.; Ding, L.; Fan, X.; Jiang, W.; Gong, X., A Liquid Metal-based Triboelectric Nanogenerator as Stretchable Electronics for Safeguarding and Self-powered Mechanosensing. *Nano Energy* **2018,** *53*, 863-870.

93. Li, H.; Wang, Z.; Lu, S.; Ma, Y.; Feng, X., Elastomers with Microislands as Strain Isolating Substrates for Stretchable Electronics. *Adv. Mater. Technol.* **2019,** *4* (2), 1800365.

94. Prasad Sahoo, B.; Naskar, K.; Kumar Tripathy, D., Multiwalled Carbon Nanotube - filled Ethylene Acrylic Elastomer Nanocomposites: Influence of Ionic Liquids

on the Mechanical, Dynamic Mechanical, and Dielectric Properties. *Polym. Compos.* **2016,** *37* (8), 2568-2580.

95. Oh, K.; Lee, J. Y.; Lee, S.-S.; Park, M.; Kim, D.; Kim, H., Highly Stretchable Dielectric Nanocomposites Based on Single-walled Carbon Nanotube/Ionic Liquid Gels. *Compos. Sci. Technol.* **2013,** *83*, 40-46.

96. Fritzsche, J.; Lorenz, H.; Klüppel, M.; Das, A.; Jurk, R.; Stöckelhuber, K.; Heinrich, G., Elastomer–Carbon Nanotube Composites. In *Polymer–Carbon Nanotube Composites*, Elsevier: 2011; pp 193-229.

97. Fukushima, T.; Aida, T., Ionic Liquids for Soft Functional Materials with Carbon Nanotubes. *Chem. Eur. J* **2007,** *13* (18), 5048-5058.

98. Fukushima, T.; Kosaka, A.; Ishimura, Y.; Yamamoto, T.; Takigawa, T.; Ishii, N.; Aida, T., Molecular Ordering of Organic Molten Salts Triggered by Single-walled Carbon Nanotubes. *Science* **2003,** *300* (5628), 2072-2074.

99. Das, A.; Stöckelhuber, K. W.; Jurk, R.; Fritzsche, J.; Klüppel, M.; Heinrich, G., Coupling Activity of Ionic Liquids Between Diene Elastomers and Multi-walled Carbon Nanotubes. *Carbon* **2009,** *47* (14), 3313-3321.

100. Kreyenschulte, H.; Richter, S.; Götze, T.; Fischer, D.; Steinhauser, D.; Klüppel, M.; Heinrich, G., Interaction of 1-allyl-3-methyl-imidazolium Chloride and Carbon Black and Its Influence on Carbon Black Filled Rubbers. *Carbon* **2012,** *50* (10), 3649-3658.

101. Steinhauser, D.; Subramaniam, K.; Das, A.; Heinrich, G.; Klüppel, M., Influence of Ionic Liquids on the Dielectric Relaxation Behavior of CNT Based Elastomer Nanocomposites. *Express Polym. Lett.* **2012,** *6* (11), 927–936.

102. Hassouneh, S. S.; Yu, L.; Skov, A. L.; Daugaard, A. E., Soft and Flexible Conductive PDMS/MWCNT Composites. *J. Appl. Polym. Sci.* **2017,** *134* (18), 44767.

103. Narongthong, J.; Das, A.; Le, H. H.; Wießner, S.; Sirisinha, C., An Efficient Highly Flexible Strain Sensor: Enhanced Electrical Conductivity, Piezoresistivity and Flexibility of a Strongly Piezoresistive Composite Based on Conductive Carbon Black and an Ionic Liquid. *Compos. Part A Appl. Sci. Manuf.* **2018,** *113*, 330-338.

104. Narongthong, J.; Le, H. H.; Das, A.; Sirisinha, C.; Wießner, S., Ionic Liquid Enabled Electrical-Strain Tuning Capability of Carbon Black Based Conductive Polymer Composites for Small-Strain Sensors and Stretchable Conductors. *Compos. Sci. Technol.* **2019,** *174*, 202-211.

105. Hunt, A.; Ewing, R., Percolation Theory: Topology and Structure. In *Percolation Theory for Flow in Porous Media*, Springer Berlin Heidelberg: Berlin, Heidelberg, 2009; pp 1-36.

106. Bunde, A.; Kantelhardt, J. W., Diffusion and Conduction in Percolation Systems. In *Diffusion in Condensed Matter: Methods, Materials, Models*, Heitjans, P.; Kärger, J., Eds. Springer Berlin Heidelberg: Berlin, Heidelberg, 2005; pp 895-914.

107. Kirkpatrick, S., Percolation and Conduction. *Rev. Mod. Phys.* **1973,** *45* (4), 574-588.

108. Broadbent, S. R.; Hammersley, J. M., Percolation Processes. *Math. Proc. Cambridge Philos. Soc.* **2008,** *53* (3), 629-641.

109. Dang, Z.-M.; Shehzad, K.; Zha, J.-W.; Mujahid, A.; Hussain, T.; Nie, J.; Shi, C.-Y., Complementary Percolation Characteristics of Carbon Fillers Based Electrically Percolative Thermoplastic Elastomer Composites. *Compos. Sci. Technol.* **2011,** *72* (1), 28-35.

110. Sahimi, M.; Hughes, B. D.; Scriven, L. E.; Davis, H. T., Critical Exponent of Percolation Conductivity by Finite-Size Scaling. *J. Phys. C: Solid State Phys.* **1983,** *16* (16), L521.

111. Rubin, Z.; Sunshine, S. A.; Heaney, M. B.; Bloom, I.; Balberg, I., Critical Behavior of The Electrical Transport Properties in a Tunneling-Percolation System. *Phys. Rev. B* **1999,** *59* (19), 12196-12199.

112. Consiglio, R.; Baker, D. R.; Paul, G.; Stanley, H. E., Continuum Percolation Thresholds for Mixtures of Spheres of Different Sizes. *Phys. A* **2003,** *319*, 49-55.

113. Battisti, A.; Skordos, A. A.; Partridge, I. K., Percolation Threshold of Carbon Nanotubes Filled Unsaturated Polyesters. *Compos. Sci. Technol.* **2010,** *70* (4), 633-637.

114. Fang, Y.; Hu, S.; Li, L.-y.; Jang, S.-H., Percolation Threshold and Effective Properties of CNTs-Reinforced Two-Phase Composite Materials. *Mater. Today Commun.* **2021,** *29*, 102977.

115. Bauhofer, W.; Kovacs, J. Z., A Review and Analysis of Electrical Percolation in Carbon Nanotube Polymer Composites. *Compos. Sci. Technol.* **2009,** *69* (10), 1486-1498.

116. Celzard, A.; McRae, E.; Deleuze, C.; Dufort, M.; Furdin, G.; Marêché, J. F., Critical Concentration in Percolating Systems Containing a High-Aspect-Ratio Filler. *Phys. Rev. B* **1996,** *53* (10), 6209-6214.

117. Mohan, L.; Kumar, P. N.; Karakkad, S.; Krishnan, S. T., Determination of Electrical Percolation Threshold of Carbon Nanotube-Based Epoxy Nanocomposites and Its Experimental Validation. *IET Sci., Meas. Technol.* **2019,** *13* (9), 1299-1304.

118. Chen, Y.; Pan, F.; Guo, Z.; Liu, B.; Zhang, J., Stiffness Threshold of Randomly Distributed Carbon Nanotube Tetworks. *J. Mech. Phys. Solids* **2015,** *84*, 395-423.

119. Oseli, A.; Tomković, T.; Hatzikiriakos, S. G.; Vesel, A.; Arzenšek, M.; Rojac, T.; Mihelčič, M.; Slemenik Perše, L., Carbon Nanotube Network Formation and Configuration/Morphology on Reinforcing and Conductive Performance of Polymer-Based Nanocomposites. *Compos. Sci. Technol.* **2023,** *237*, 110010.

120. Schilling, T.; Miller, M. A.; Van der Schoot, P., Percolation in Suspensions of Hard Nanoparticles: from Spheres to Needles. *EPL (Europhysics Letters)* **2015,** *111* (5), 56004.

121. Choi, H. J.; Kim, M. S.; Ahn, D.; Yeo, S. Y.; Lee, S., Electrical Percolation Threshold of Carbon Black in a Polymer Matrix and Its Application to Antistatic Fibre. *Sci. Rep.* **2019,** *9*, 6338.

122. Grujnlan, J. C.; Gerberich, W. W.; Francis, L. F., Lowering The Percolation Threshold In Carbon Blackfilled Polymer Composites. *MRS Online Proc. Libr.* **1999,** *576* (1), 383-387.

123. Pelíšková, M.; Piyamanocha, P.; Prokeš, J.; Varga, M.; Sáha, P., The electrical Conductivity of Ethylene Butyl-Acrylate/Carbon Black Composites: the Effect of Foaming on the Percolation Threshold. *Synth. Met.* **2014,** *188*, 140-145.

124. Premphet, K.; Horanont, P., Phase Structure and Property Relationships in Ternary Polypropylene/Elastomer/Filler composites: Effect of Elastomer Polarity. *J. Appl. Polym. Sci.* **2000,** *76* (13), 1929-1939.

125. Zhang, Y.-C.; Zheng, D.; Pang, H.; Tang, J.-H.; Li, Z.-M., The Effect of Molecular Chain Polarity on Electric Field-induced Aligned Conductive Carbon Nanotube Network Formation in Polymer Melt. *Compos. Sci. Technol.* **2012,** *72* (15), 1875-1881.

126. Huynh, M. T. T.; Cho, H.-B.; Suzuki, T.; Suematsu, H.; Nguyen, S. T.; Niihara, K.; Nakayama, T., Electrical Property Enhancement by Controlled Percolation Structure of Carbon Black in Polymer-based Nanocomposites *via* Nanosecond Pulsed Electric Field. *Compos. Sci. Technol.* **2018,** *154*, 165-174.

127. Kontopoulou, M.; Kaufman, M.; Docoslis, A., Electrorheological Properties of PDMS/Carbon Black Suspensions Under Shear Flow. *Rheol. Acta* **2008,** *48* (4), 409-421.

128. Huang, J.; Mao, C.; Zhu, Y.; Jiang, W.; Yang, X., Control of Carbon Nanotubes at the Interface of a Co-continuous Immiscible Polymer Blend to Fabricate Conductive Composites With Ultralow Percolation Thresholds. *Carbon* **2014,** *73*, 267-274.

129. Krause, B.; Boldt, R.; Häußler, L.; Pötschke, P., Ultralow Percolation Threshold in Polyamide 6.6/MWCNT Composites. *Compos. Sci. Technol.* **2015,** *114*, 119-125.

130. Wang, D.; Zhang, X.; Zha, J.-W.; Zhao, J.; Dang, Z.-M.; Hu, G.-H., Dielectric Properties of Reduced Graphene Oxide/Polypropylene Composites with Ultralow Percolation Threshold. *Polymer* **2013,** *54* (7), 1916-1922.

131. Ju, J.; Kuang, T.; Ke, X.; Zeng, M.; Chen, Z.; Zhang, S.; Peng, X., Lightweight Multifunctional Polypropylene/Carbon Nanotubes/Carbon Black Nanocomposite Foams with Segregated Structure, Ultralow Percolation Threshold and Enhanced Electromagnetic Interference Shielding Performance. *Compos. Sci. Technol.* **2020,** *193*, 108116.

132. Sumita, a.; Sakata, K.; Hayakawa, Y.; Asai, S.; Miyasaka, K.; Tanemura, M., Double Percolation Effect on the Electrical Conductivity of Conductive Particles Filled Polymer Blends. *Colloid Polym. Sci.* **1992,** *270* (2), 134-139.

133. Mamunya, Y. P., Morphology and Percolation Conductivity of Polymer Blends Containing Carbon Black. *J. Macromol. Sci., Part B: Phys.* **1999,** *38* (5-6), 615-622.

134. Lee, G. J.; Suh, K. D.; Im, S. S., Effect of Incorporating Ethylene - Ethylacrylate Copolymer on The Positive Temperature Coefficient Characteristics of Carbon Black Filled HDPE Systems. *Polym. Eng. Sci.* **2000,** *40* (1), 247-255.

135. Tchoudakov, R.; Breuer, O.; Narkis, M.; Siegmann, A., Conductive Polymer Blends with Low Carbon Black Loading: Polypropylene/Polyamide. *Polym. Eng. Sci.* **1996,** *36* (10), 1336-1346.

136. Huang, J.-C.; Wu, C.-L.; Grossman, S. J., Carbon Black-Filled Conductive Polymers of Polypropylene, Ethylene Vinyl Acetate Copolymer, and Their Ternary Blends. *J. Polym. Eng.* **2000,** *20* (3), 213-223.

137. Jäger, K.-M.; McQueen, D. H., Fractal Agglomerates and Electrical Conductivity in Carbon Black Polymer Composites. *Polymer* **2001,** *42* (23), 9575-9581.

138. Fleischmann, M.; Tildesley, D. J.; Ball, R., *Fractals in the Natural Sciences*. Princeton University Press: 2014; Vol. 1083.

139. Pfeifer, P.; Obert, M.; Cole, M., Fractal BET and FHH Theories of Adsorption: A Comparative Study. *Proc. R. Soc. London, Ser. A* **1989,** *423* (1864), 169-188.

140. Pfeifer, P.; Wu, Y. J.; Cole, M. W.; Krim, J., Multilayer Adsorption on a Fractally Rough Surface. *Phys. Rev. Lett.* **1989,** *62* (17), 1997-2000.

141. Pfeifer, P., Fractal Dimension as Working Tool for Surface-roughness Problems. *Appl. Surf. Sci.* **1984,** *18* (1), 146-164.

142. Svedberg, T.; Rinde, H., The Ultra-Centrifuge, a New Instrument for the Determination of Size and Distribution of Size of Particle in Amicroscopic Colloids. *J. Am. Chem. Soc.* **2002,** *46* (12), 2677-2693.

143. Hodoroaba, V.-D.; Unger, W.; Shard, A., *Characterization of Nanoparticles: Measurement Processes for Nanoparticles*. Elsevier: 2019.

144. Mächtle, W.; Börger, L., *Analytical Ultracentrifugation of Polymers and Nanoparticles*. Springer Science & Business Media: 2006.

145. Cölfen, H.; Wohlleben, W., *Analytical Ultracentrifugation of Latexes*. 2010.

146. Chiu, H.-T.; Chang, C.-Y.; Chiang, T.-Y.; Kuo, M.-T.; Wang, Y.-H., Using Analytical Centrifugation to Characterize the Dispersibility and Particle Size Distributions of Organic/Inorganic Composite Coatings. *J. Polym. Res.* **2011,** *18* (6), 1587-1596.

147. Detloff, T.; Sobisch, T.; Lerche, D., Particle Size Distribution by Space or Time Dependent Extinction Profiles Obtained by Analytical Centrifugation. *Part. Part. Syst. Charact.* **2006,** *23* (2), 184-187.

148. Wriedt, T., Mie Theory: A Review. In *The Mie Theory: Basics and Applications*, Hergert, W.; Wriedt, T., Eds. Springer Berlin Heidelberg: Berlin, Heidelberg, 2012; pp 53-71.

149. Taherian, R., 1 - The Theory of Electrical Conductivity. In *Electrical Conductivity in Polymer-Based Composites*, Taherian, R.; Kausar, A., Eds. William Andrew Publishing: 2019; pp 1-18.

150. Shen, L.; Li, J.; Liaw, B. M.; Delale, F.; Chung, J. H., Modeling and analysis of the electrical resistance measurement of carbon fiber polymer–matrix composites. *Compos. Sci. Technol.* **2007,** *67* (11-12), 2513-2520.

151. Miccoli, I.; Edler, F.; Pfnur, H.; Tegenkamp, C., The 100th Anniversary of the Four-point Probe Technique: the Role of Probe Geometries in Isotropic and Anisotropic Systems. *J. Phys.: Condens. Matter* **2015,** *27* (22), 223201.

152. Smits, F. M., Measurement of Sheet Resistivities with the Four-Point Probe. *Bell Syst. Tech. J.* **1958,** *37* (3), 711-718.

153. Seeck, O. H.; Murphy, B., *X-ray Diffraction: Modern Experimental Techniques*. CRC Press: 2015.

154. de Jeu, W. H., *Basic X-Ray Scattering for Soft Matter*. Oxford University Press: 2016.

155. Rishi, K.; Beaucage, G.; Kuppa, V.; Mulderig, A.; Narayanan, V.; McGlasson, A.; Rackaitis, M.; Ilavsky, J., Impact of an Emergent Hierarchical Filler Network on Nanocomposite Dynamics. *Macromolecules* **2018,** *51* (20), 7893-7904.

156. Rishi, K.; Pallerla, L.; Beaucage, G.; Tang, A., Dispersion of Surface-modified, Aggregated, Fumed Silica in Polymer Nanocomposites. *J. Appl. Phys.* **2020,** *127* (17), 174702.

157. Beaucage, G., Approximations Leading to a Unified Exponential/Power-Law Approach to Small-Angle Scattering. *J. Appl. Crystallogr.* **1995,** *28* (6), 717-728.

158. Beaucage, G., Small-Angle Scattering from Polymeric Mass Fractals of Arbitrary Mass-Fractal Dimension. *J. Appl. Crystallogr.* **1996,** *29* (2), 134-146.

159. Gottlieb, M., Swelling of Polymer Networks. In *Biological and Synthetic Polymer Networks*, Kramer, O., Ed. Springer Netherlands: Dordrecht, 1988; pp 403-414.

160. Flory, P. J., Thermodynamics of High Polymer Solutions. *J. Chem. Phys.* **2004,** *10* (1), 51-61.

161. Huggins, M. L., Solutions of Long Chain Compounds. *J. Chem. Phys.* **2004,** *9* (5), 440-440.

162. Flory, P. J., Molecular Theory of Rubber Elasticity. *Polym. J.* **1985,** *17* (1), 1-12.

163. Sannino, A.; Madaghiele, M.; Ambrosio, L., 5 - Biocompatibility and Other Properties of Hydrogels in Regenerative Medicine. In *Cell. Response Biomater.*, Di Silvio, L., Ed. Woodhead Publishing: 2009; pp 114-135.

164. Bastola, A. K.; Hossain, M., A Review on Magneto-Mechanical Characterizations Of Magnetorheological Elastomers. *Composites, Part B* **2020,** *200*, 108348.

165. Bokobza, L., Mechanical and Electrical Properties of Elastomer Nanocomposites Based on Different Carbon Nanomaterials. *C* **2017,** *3* (2), 10.

166. Robertson, C. G.; Hardman, N. J., Nature of Carbon Black Reinforcement of Rubber: Perspective on the Original Polymer Nanocomposite. *Polymers* **2021,** *13* (4), 538.

167. Franta, I., *Elastomers and Rubber Compounding Materials*. Elsevier: 2012; Vol. 1.

168. Willenbacher, N.; Georgieva, K., Rheology of Disperse Systems. In *Product Design and Engineering*, 2013; pp 7-49.

169. Mezger, T., *The Rheology Handbook: For Users of Rotational And Oscillatory Rheometers*. Vincentz Network: 2014.

170. Goodwin, J. W.; Hughes, R. W., *Rheology for Chemists: An Introduction*. Royal Society of Chemistry: 2008.

171. Süß, S.; Sobisch, T.; Peukert, W.; Lerche, D.; Segets, D., Determination of Hansen Parameters for Particles: A Standardized Routine Based on Analytical Centrifugation. *Adv. Powder Technol.* **2018,** *29* (7), 1550-1561.

172. Buffet, A.; Rothkirch, A.; Dohrmann, R.; Korstgens, V.; Abul Kashem, M. M.; Perlich, J.; Herzog, G.; Schwartzkopf, M.; Gehrke, R.; Muller-Buschbaum, P.; Roth, S. V., P03, the Microfocus and Nanofocus X-ray Scattering (MiNaXS) Beamline of the PETRA III Storage Ring: the Microfocus Endstation. *J. Synchrotron Radiat.* **2012,** *19* (Pt 4), 647-53.

173. Egger, C. C.; du Fresne, C.; Raman, V. I.; Schadler, V.; Frechen, T.; Roth, S. V.; Muller-Buschbaum, P., Characterization of Highly Porous Polymeric Materials with Pore Diameters Larger Than 100 nm by Mercury Porosimetry and X-ray Scattering Methods. *Langmuir* **2008,** *24* (11), 5877-87.

174. Benecke, G.; Wagermaier, W.; Li, C.; Schwartzkopf, M.; Flucke, G.; Hoerth, R.; Zizak, I.; Burghammer, M.; Metwalli, E.; Muller-Buschbaum, P.; Trebbin, M.; Forster, S.; Paris, O.; Roth, S. V.; Fratzl, P., A Customizable Software for Fast Reduction and Analysis of Large X-ray Scattering Data Sets: Applications of the New DPDAK Package to Small-angle X-ray Scattering and Grazing-incidence Small-angle X-ray Scattering. *J. Appl. Crystallogr.* **2014,** *47* (Pt 5), 1797-1803.

175. Oles, V., Shear-Induced Aggregation and Breakup of Polystyrene Latex Particles. *J. Colloid Interface Sci.* **1992,** *154* (2), 351-358.

176. Coupette, F.; Zhang, L.; Kuttich, B.; Chumakov, A.; Roth, S. V.; Gonzalez-Garcia, L.; Kraus, T.; Schilling, T., Percolation of Rigid Fractal Carbon Black Aggregates. *J. Chem. Phys.* **2021,** *155* (12), 124902.

177. Medalia, A. I., Electrical Conduction In Carbon Black Composites. *Rubber Chem. Technol.* **1986,** *59* (3), 432-454.

178. Thovert, J. F.; Mourzenko, V. V.; Adler, P. M., Percolation in Three-dimensional Fracture Networks for Arbitrary Size and Shape Distributions. *Phys. Rev. E* **2017,** *95* (4-1), 042112.

179. Ehrburger-Dolle, F.; Hindermann-Bischoff, M.; Livet, F.; Bley, F.; Rochas, C.; Geissler, E., Anisotropic Ultra-Small-Angle X-ray Scattering in Carbon Black Filled Polymers. *Langmuir* **2000,** *17* (2), 329-334.

180. Ehrburger-Dolle, F.; Morfin, I.; Bley, F.; Livet, F.; Heinrich, G.; Richter, S.; Piché, L.; Sutton, M., XPCS Investigation of the Dynamics of Filler Particles in Stretched Filled Elastomers. *Macromolecules* **2012,** *45* (21), 8691-8701.

181. Salome, L.; Carmona, F., Fractal Structure Study of Carbon Blacks Used as Conducting Polymer Fillers. *Carbon* **1991,** *29* (4-5), 599-604.

182. Peidayesh, H.; Mosnáčková, K.; Špitalský, Z.; Heydari, A.; Šišková, A. O.; Chodák, I., Thermoplastic Starch–Based Composite Reinforced by Conductive Filler Networks: Physical Properties and Electrical Conductivity Changes during Cyclic Deformation. *Polymers* **2021,** *13* (21), 3819.

183. Park, D. H.; Park, H. W.; Chung, J. W.; Nam, K.; Choi, S.; Chung, Y. S.; Hwang, H.; Kim, B.; Kim, D. H., Highly Stretchable, High - Mobility, Free - Standing All - Organic Transistors Modulated by Solid - State Elastomer Electrolytes. *Adv. Funct. Mater.* **2019,** *29* (18), 1808909.

184. Sinawang, G.; Kobayashi, Y.; Zheng, Y.; Takashima, Y.; Harada, A.; Yamaguchi, H., Preparation of Supramolecular Ionic Liquid Gels Based on Host–Guest Interactions and Their Swelling and Ionic Conductive Properties. *Macromolecules* **2019,** *52* (8), 2932-2938.

185. Ankit; Tiwari, N.; Ho, F.; Krisnadi, F.; Kulkarni, M. R.; Nguyen, L. L.; Koh, S. J. A.; Mathews, N., High-k, Ultrastretchable Self-Enclosed Ionic Liquid-Elastomer Composites for Soft Robotics and Flexible Electronics. *ACS Appl. Mater. Interfaces* **2020,** *12* (33), 37561-37570.

186. Marwanta, E.; Mizumo, T.; Nakamura, N.; Ohno, H., Improved Ionic Conductivity of Nitrile Rubber/Ionic Liquid Composites. *Polymer* **2005,** *46* (11), 3795-3800.

187. Laskowska, A.; Marzec, A.; Boiteux, G.; Zaborski, M.; Gain, O.; Serghei, A., Effect of Imidazolium Ionic Liquid Type on the Properties of Nitrile Rubber Composites. *Polym. Int.* **2013,** *62* (11), 1575-1582.

188. Zhang, X.; Xue, X.; Jia, H.; Wang, J.; Ji, Q.; Xu, Z., Influence of Ionic Liquid on the Polymer-filler Coupling and Mechanical Properties of Nano-silica Filled Elastomer. *J. Appl. Polym. Sci.* **2017,** *134* (7), 44478.

189. Shinohara, Y.; Kishimoto, H.; Inoue, K.; Suzuki, Y.; Takeuchi, A.; Uesugi, K.; Yagi, N.; Muraoka, K.; Mizoguchi, T.; Amemiya, Y., Characterization of Two-dimensional Ultra-small-angle X-ray scattering Apparatus for Application to Rubber Filled with Spherical Silica Under Elongation. *J. Appl. Crystallogr.* **2007,** *40* (s1), s397-s401.